PHYSICAL REVIEW FLUIDS **4**, 054601 (2019)

Very large-scale motions in turbulent flows over streamwise traveling wavy boundaries

Wu-Yang Zhang, Wei-Xi Huang,* and Chun-Xiao Xu
AML, Department of Engineering Mechanics, Tsinghua University, Beijing 100084, People's Republic of China

(Received 6 December 2018; published 7 May 2019)

Turbulent flows over streamwise traveling wavy boundaries are investigated by large eddy simulations at a friction Reynolds number of $\mathrm{Re}_\tau = 1000$. Four wave ages (i.e., the ratio between wave phase speed and bulk mean velocity) are considered, sequentially corresponding to the wave moving against the wind, stationary wavy wall, and intermediate and fast waves. A triple decomposition is performed to extract the mean, wave-induced, and turbulent components of the flow field. Very large-scale motions (VLSMs) of turbulent flow are identified by using the one-dimensional premultiplied energy spectra, instantaneous flow fields and conditionally averaged results. Compared with the flat-wall case, VLSMs in the negative wave age and stationary wavy wall cases are stronger, with larger length scales in both the streamwise and spanwise directions. The length scale and intensity of these motions decrease as the wave age increases. The conditionally averaged VLSMs involve the elongated low- and high-speed momentum regions and the roll cells in the streamwise direction. The transport equation of the two-point velocity correlation is investigated in different length scales by applying a spectral analysis. The wave-induced production that represents the interaction between the wave-induced and turbulent components of flow velocities provides extra input for the large-scale energy at low wave ages but play an opposite role at high wave ages.

DOI: 10.1103/PhysRevFluids.4.054601

I. INTRODUCTION

The coupling dynamic process between surface wave and turbulent flow exists widely in engineering and environmental flow phenomena and therefore is of great interest in many studies. Turbulent flow over a stationary wavy wall can be applied for heat transfer enhancement in some industrial devices [1,2]. It is also related to geophysical flows, such as oceanic flow over sandbars [3] and wind flow over wavy terrains [4]. However, turbulent flow over a surface undergoing a traveling wave motion can be considered as a control scheme for drag reduction [5–7]. This system has also been widely used as an idealized model of wind flowing over water surface in environmental research, such as energy transfer from wind to wave [8–11], wind-wave interaction [12–15], heat/mass mixing and exchange between atmosphere and sea [16–19]), and wind over breaking waves [20]. The previous studies showed that there were substantial differences between the turbulent flow over the wavy boundary and that over the flat wall. The influences of the surface wave on the turbulent momentum [12] and scalar [19] transport have complicated dependence on the geometry, length scale, and kinematics of the surface wave. Some open questions, such as applicability of the turbulence scaling law and estimation of the drag and mass/heat flux, are the key issues in the practical fields, e.g., the turbulence closure model in wavy boundary flow

---

[*] hwx@tsinghua.edu.cn

[21,22], surface model for large-eddy simulation [23,24], and climate forecast model [25,26]. Thus, quantitative examination of the surface wave effects on turbulence and understanding of the underlying mechanism are challenging work and have important value of application.

In the past few decades, extensive studies have been performed on turbulent flow over wavy boundaries. Several theoretical models of the wave growth rate were developed, e.g., Miles [8], Belcher and Hunt [10], and Cohen and Belcher [11]. According to these theories, the energy exchange between air and wave is directly influenced by the phase speed of the surface wave, which affects not only the height of the critical layer, where the mean wind speed equals the wave phase speed but also the wave-induced and Reynolds stresses. The normalized phase speed is also used to describe the age of the ocean waves [27] and is usually referred to as the wave age. These theories had been supported by both numerical and experimental studies. Sullivan *et al.* [12], Kihara *et al.* [28], and Yang and Shen [14] studied the wave-induced flow and Reynolds stresses for flow over moving wavy boundaries with various wave ages by using direct numerical simulation (DNS). In their results, the sign, intensity, and spatial distribution of the wave-induced and Reynolds stresses in the vicinity of the surface are significantly affected by the wave age. More recently, further extensions to higher Reynolds numbers with a wide range of wave ages by using large-eddy simulation (LES) can be found in Sullivan *et al.* [13], Hara and Sullivan [15], and Jiang *et al.* [29]. The effects of wave age on the wave-induced and turbulent momentum flux were also carefully measured in the laboratory [30].

In addition, various studies have been conducted on the interaction between the wave-induced flow and turbulent fluctuations. Reynolds and Hussain [12] derived the transport equations of the averaged energies of both the wave-induced and turbulent fluctuations based on a triple decomposition. The cross term in their equations indicates the interaction between these two components. Yang and Shen [14] added the cross term and the production term as a whole input of the TKE and then explained the distribution of the Reynolds stresses near the wave surface. While in an earlier research [31], Yang and Shen reported that turbulent coherent vortices in the wavy boundary turbulence have different orientations and preferential concentration depending on the phase of waves at different wave ages. Combining the phase-dependent wave-induced fluctuation with turbulent coherent vortices, they provided a physical mechanism of the interaction between the wave-induced and turbulent fluctuations. Zedler and Street [3], Choi *et al.* [32], Tseng and Ferziger [33], and Wagner *et al.* [34] also discussed the wave effect on the turbulent coherent structures.

The classic coherent structures in the near-wall turbulence, such as low-speed streaks and quasistreamwise vortices, have been widely investigated [35] and their geometric features scale with the inner scale in wall viscous units [36,37]. In recent years, the very large-scale motions (VLSMs) scale with the outer scale, such as the half-channel height or the boundary layer thickness, in the logarithmic region of the flat-wall turbulence were observed at high Reynolds-number flows [38–40]. It was reported that at high Reynolds numbers, the VLSMs contribute more than half of the Reynolds shear stress [41]. Moreover, the VLSMs superimpose their footprints on near-wall fluctuations and have an amplitude modulation on the small-scale fluctuation [42,43]. In general, these VLSMs involve elongated low- and high-speed momentum regions in the streamwise direction accompanied by the large-scale roll cells between them [42,44]. These works showed that the VLSMs play an important role in the turbulent energy transport and its influence can extend throughout the whole boundary layer. The VLSMs were also widely reported in the turbulent Couette flow [45–47] at relatively low Reynolds numbers.

Interestingly, the enhanced and enlarged flow structures were observed in the previous studies of flow over a stationary wavy wall. Early examples include De Angelis *et al.* [48] using DNS and Henn and Sykes [49] using LES, where the vortexlike enhanced transverse flow was presented. Meanwhile, Gong *et al.* [50] also observed the vortex pairs aligned with the mean flow in their laboratory experiment and mentioned that the vortex scaled with the boundary layer thickness. Günther and Von Rohr [51], and Kruse *et al.* [52,53] performed experiments of a turbulent channel flow over the static waves at the bottom wall. They applied a proper orthogonal decomposition (POD) to the streamwise velocity fluctuation and extracted a dominant flow structure with a spanwise scale of 1.5 times of the full channel height. In their subsequent studies, the intensity and characteristic spanwise scale of the large-scale structures increase with the blockage ratio, i.e., the ratio of the wave amplitude to the full channel height [54,55]. However, very large-scale structures in turbulent flow over moving waves were also investigated in some work of the marine-atmosphere boundary layer (MABL). Nilsson *et al.* [56] reported that the VLSMs in the boundary layer were disrupted by the wave at high wave ages. Sullivan *et al.* [57] observed the very large-scale streaky structures in the MABL above the broadband waves and discussed their impacts on the local wave age. However, these works usually contained other physical mechanisms in the MABL, such as broadband waves, buoyancy, and earth rotation, which make the problem become more complicated.

As seen above, both the experimental and numerical works provided the evidence that wavy boundary has impacts on the VLSMs at high Reynolds numbers. So far, the very large-scale structures in the stationary wavy wall flow had been widely studied, while the related research for the traveling wave is scarce. Further study on the influence of the geometric and phase speed of waves on the VLSMs in turbulence is still needed, and the underlying mechanism is still to be explored.

In the present work, we simulate the turbulent flow over traveling waves by using LES and mainly focus on the influence of the wave on the VLSMs in the outer layer. The wall-resolved LES is performed to catch the large-scale turbulent motions at a moderate friction Reynolds number, i.e., $\mathrm{Re}_\tau \approx 1000$. Four wave ages are examined, and a comparatively small wave steepness is chosen. To identify the wave-turbulence interaction, phase average and triple decomposition [12] are adopted in the analysis of the flow field. The significantly enhanced VLSMs by the wave are observed in the spanwise energy spectra of Reynolds stresses. Instantaneous snapshots and conditional average are also applied to illustrate the very large-scale structures. Following the study on the inner-outer interaction of Lee [58], we applied a spectral analysis of the transport equation of the two-point velocity correlation, to elucidate the mechanism of the enhancement of the VLSMs by the wave. The paper is organized as follows. The problem definition, numerical method, and analysis procedure are briefly described in Sec. II. In Sec. III, the turbulence statistics and VLSMs are introduced, the spectral analysis on the transport equation of the two-point velocity correlation are carried out, and the effects of wave steepness and Reynolds number are also discussed. Finally, conclusions are drawn in Sec. IV.

II. PROBLEM FORMULATION AND NUMERICAL METHOD

A. Flow configuration and governing equations

The problem considered here is the fully developed three-dimensional open-channel turbulent flow over the wave traveling in the streamwise direction. A sketch of the computational domain and coordinate system is shown in Fig. 1. The flow is driven by an averaged streamwise gradient of pressure which is dynamically adjusted and makes the flow rate to be strictly constant in time. We adopt a Cartesian frame fixed in the physical space, with x, y, z being the streamwise, vertical, and spanwise coordinates (also denoted as x_1, x_2, and x_3 for the tensor notation). The corresponding velocity components in the three directions are u, v, and w (or u_1, u_2, and u_3), respectively. The resolvable turbulent flow field is described by the filtered incompressible Navier-Stokes equations and the continuity equation, i.e.,

$$\frac{\partial u_i}{\partial x_i} = 0, \tag{1}$$

$$\frac{\partial u_i}{\partial t} + u_j \frac{\partial u_i}{\partial x_j} = -\frac{\partial p}{\partial x_i} + \frac{1}{\mathrm{Re}_b} \frac{\partial^2 u_i}{\partial x_j \partial x_j} - \frac{\partial \tau_{ij}^d}{\partial x_j}. \tag{2}$$

Here $u_i (i = 1, 2, 3) = (u, v, w)$ are the filtered velocity components, and p is the modified pressure which consists of the filtered static pressure and the subgrid-scale (SGS) kinetic energy. The governing equations are nondimensionalized by using the bulk velocity U_b, fluid density ρ, open-channel height δ, and the kinematic viscosity ν as the characteristic quantities. The bulk

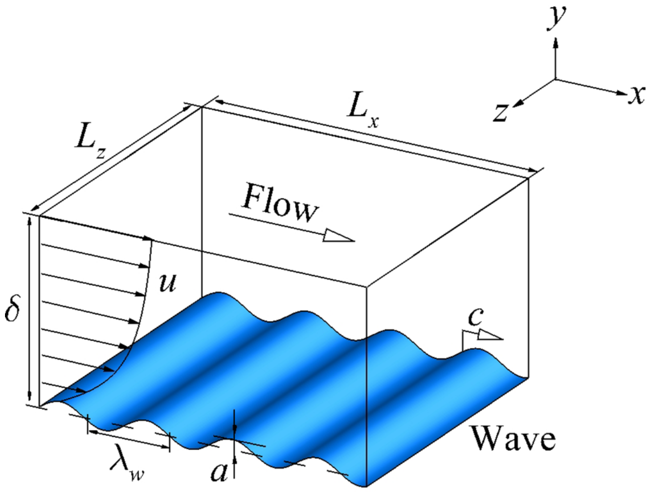

FIG. 1. Sketch of the turbulent open-channel flow over a traveling wavy boundary.

velocity is defined as $U_b = Q/\delta$, where Q denotes the volume flow rate. The bulk Reynolds number is defined as $\mathrm{Re}_b = U_b\delta/\nu$. τ_{ij}^d is the trace-free part of the SGS stress which is modelled by using the dynamic Smagorinsky model [59,60] including a spanwise averaged model coefficient.

B. Boundary conditions and simulation parameters

In the open-channel flow, a free-slip wall is applied at the top boundary ($y = \delta$) of the computational domain,

$$\left.\frac{\partial u}{\partial y}\right|_{y=\delta} = 0, \quad v|_{y=\delta} = 0, \quad \left.\frac{\partial w}{\partial y}\right|_{y=\delta} = 0. \tag{3}$$

This condition also means that there is no momentum flux in the vertical direction at the top boundary. The periodic condition is applied in the streamwise and spanwise directions. At the bottom boundary, the idealized water wave is prescribed by the two-dimensional monochrome streamwise traveling wave. In the present study, the averaged bottom boundary is located at $y = 0$, and the deformation of the wave surface η_d and the vertical location of the surface y_d are controlled by

$$y_d = \eta_d = a\sin[k_w(x - ct)]. \tag{4}$$

Here a is the wave amplitude, $k_w = 2\pi/\lambda_w$ is the wave number with λ_w the wavelength, and c is the wave phase speed. The orbital velocity at the wave surface is used as the Dirichlet boundary condition for the turbulent flow, i.e.,

$$(u_w, v_w, w_w) = (ak_wc\sin[k_w(x - ct)], \quad -ak_wc\cos[k_w(x - ct)], 0). \tag{5}$$

In our simulation, the wave slope is small but finite, i.e., $ak_w = 0.1$. The influence of the wave age is investigated by changing the ratio between the wave phase speed c and the bulk velocity U_b. The bulk velocity is kept constant in simulation and is slightly lower (no more than 10%) than the mean streamwise velocity at the top boundary for all the cases with different wave ages. Hence, it can be regarded as a mean velocity far above the waves. We choose four different wave ages, namely, $c/U_b = -0.4$, 0, 0.4, and 1.2, corresponding to the wave propagating against the flow, stationary wavy wall, intermediate and fast waves [61]. The results of the open-channel with a flat wall ($a = 0$) are also shown for comparison. The characteristic friction velocity defined by the time- and surface-averaged total drag at wave surface including the friction drag and the pressure drag is expressed

TABLE I. Wave parameters and Reynolds numbers.

Boundary type	ak_w	a/δ	a^+	λ/δ	λ_w^+	c/U_b	c^+	Re_b	Re_τ
Flat wall	0	0	0					21 000	1045
Wavy boundary	0.1	0.05	51		3204	−0.4	−7.07	18 000	1020
			53	π	3330	0	0	19 000	1060
			55		3455	0.4	7.25	20 000	1100
			56		3487	1.2	23.77	22 000	1110

as $u_\tau = \sqrt{\tau_w/\rho}$. The friction Reynolds number Re_τ based on u_τ and the open-channel height δ is about 1000. Hereafter, the superscript "+" denotes the physical quantities normalized by the friction velocity u_τ and the wall viscous length scale v/u_τ. A list of Reynolds numbers and wave parameters for the different cases can be found in Table I.

C. Coordinate transformation and numerical method

To discretize the nonrectangular physical domain with a wavy boundary, a boundary-fitted grid system in the Cartesian coordinates (t, x, y, z) is applied in the physical space as shown in Fig. 2(a). Then a new computational coordinate system is introduced by adopting an algebraic mapping [62,63], i.e.,

$$t = \tau, \quad x_1 = \xi_1, \quad x_2 = \xi_2(1 - \eta_d/\delta) + \eta_d, \quad x_3 = \xi_3. \tag{6}$$

With this coordinate transformation, the irregular physical domain is transformed into a rectangular computational domain as shown in Fig. 2(b). In the computational space, the top and bottom boundaries can be represented by $\xi_2 = 0$ and $\xi_2 = \delta$, respectively. By applying the chain rule of partial derivatives, the governing Eqs. (1) and (2) are rewritten in terms of the curvilinear coordinates $(\tau, \xi_1, \xi_2, \xi_3)$ in the computational space [63]. For spatial discretization, we use the pseudo-spectral method in the ξ_1 and ξ_3 directions, along with the second-order finite-difference method on the staggered grids in the ξ_2 direction [31]. The governing equations are integrated in time by the third-order time-splitting method [64]. The computational domain size is $L_x \times L_y \times L_z = 4\pi\delta \times \delta \times 2\pi\delta$, and the corresponding grid number is $288 \times 144 \times 288$. The grid sizes in the streamwise and spanwise directions are uniform with the resolution of $\Delta\xi_1^+ \approx 45$ and $\Delta\xi_3^+ \approx 22.5$, respectively. The vertical grid size changes from $\Delta\xi_2^+ \approx 0.05$ clustered near the bottom boundary to $\Delta\xi_2^+ \approx 10$ near the top boundary.

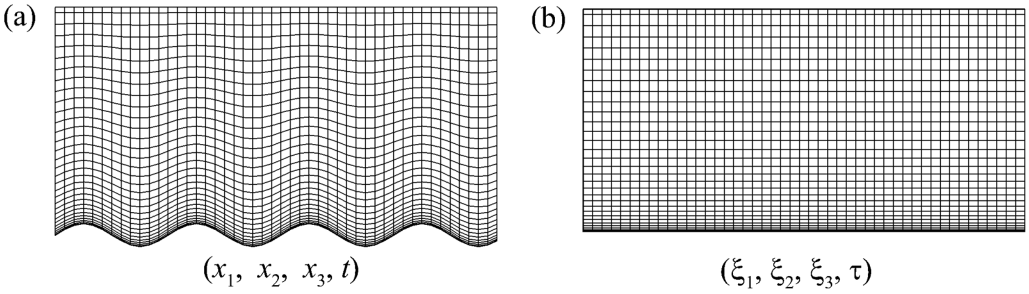

FIG. 2. Illustration of the coordinate transformation: (a) boundary-fitted grid system of the irregular domain in the physical space; (b) mapped grid system of rectangular domain in the computational space.

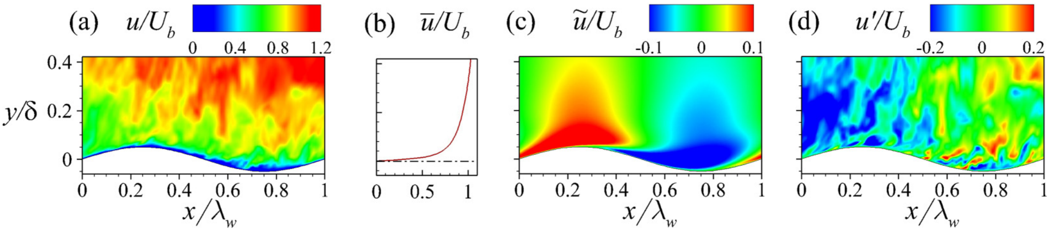

FIG. 3. Triple decomposition of the streamwise velocity: (a) instantaneous field; (b) mean profile; (c) wave-induced fluctuation; (d) turbulent fluctuation.

D. Analysis procedures

To investigate the interaction between the waves and turbulent flow, we apply a phase average and decomposition method [12] to isolate the wave-induced and turbulent fluctuations. In the present work, both the Cartesian and a surface-fitted coordinate systems defined in Eq. (6) are used in the statistical analysis [19]. By applying the average and decomposition defined in Appendix A, an instantaneous physical quantity $f(t, x, y, z)$ can be decomposed as

$$f(t, x, y, z) = \langle f \rangle(x, y) + f'(t, x, y, z) = \bar{f}(\xi_2(x, y)) + \tilde{f}(x, y) + f'(t, x, y, z), \tag{7}$$

where $\bar{f}$ denotes the time and ξ_2-plane [Eq. (6)] average, $\langle f \rangle$ denotes the phase averaged component, while $\tilde{f}$ and f' denote the wave-induced and turbulent fluctuations, respectively. As defined in Appendix A, the phase average $\langle f \rangle$ is calculated by averaging in time and along the spanwise direction, and further averaging among all the wave periods in the computational domain. The average profile $\bar{f}$ can be obtained by averaging $\langle f \rangle$ along the ξ_1-curves. Note that $\bar{f}$ is a function of ξ_2, which represents the mean vertical distance from the wave surface, i.e., $\bar{y} = \xi_2$. When the wave steepness tends to zero, the averaged profile $\bar{f}(\bar{y})$ becomes the same as the mean profile defined in the flat-wall turbulence. Hereinafter, $\bar{f}$ is referred to as the mean of f for simplification. The wave-induced fluctuation $\tilde{f}$ is obtained by subtracting $\bar{f}$ from $\langle f \rangle$ at the corresponding $\bar{y}$ location. We use Cartesian frame when describing the distributions of $\langle f \rangle$ and $\tilde{f}$. While introducing the boundary-fitted curvilinear system is appropriate for describing $\bar{f}$ in the vicinity of the wave surface, including the region below the wave crest. An example of this triple decomposition of the streamwise velocity field obtained from the stationary wavy wall case is displayed in Fig. 3. Similar triple decomposition approaches have been wildly used in previous works [12,15,19,28,30].

III. RESULTS AND DISCUSSIONS

A. Wave effect on turbulence statistics

The influence of water waves on the mean velocity profile has been widely studied due to its importance in practical applications. For example, the validity of the log law, parameterization of the wave effect on the Karman constant, and the wave surface roughness are important aspects in the ocean surface wall model [24]. In the present work, the mean streamwise velocity profiles for various wave ages are plotted in the semilogarithmic coordinates as shown in Fig. 4. Similar to the flat-wall case, all the profiles with different wave ages exhibit a logarithmic variation beyond $\bar{y}^+ = 80$. The influences of wave age on the slope and intercept of velocity profile are considerable. As the wave age increases, the profile shifts downward firstly and then upwards close to the flat-wall case. Correspondingly, the form drag of wave increases with the wave age at low wave ages and then decreases at high wave ages. The slope of velocity profile increases with the wave age, which indicates that the corresponding Karman constant of log law decreases. This trend is consistent with the results reported by Sullivan *et al.* [12] and Yang and Shen [19]. The intercept of velocity profile, which determines the efficient wave roughness, depends on the expected range where the log law is

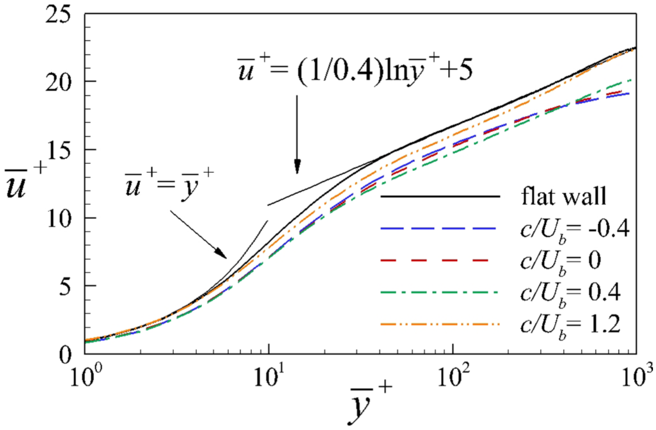

FIG. 4. Profiles of the mean streamwise velocity for different wave ages as well as the flat-wall turbulence.

satisfied and the value of the Karman constant. The results reported in previous numerical studies showed that both the Karman constant and the roughness length had complex relationships with the wave age and wave steepness [12,19,29]. This open question is beyond our current focus and needs further study.

The traveling wave motion induces a significant effect on the velocity fluctuation. According to the triple decomposition defined by Eq. (7), the mean of the momentum flux can be decomposed into three parts, i.e.,

$$\overline{u_i u_j} = \overline{(\bar{u}_i + \tilde{u}_i + u_i')(\bar{u}_j + \tilde{u}_j + u_j')} = \bar{u}_i \bar{u}_j + \overline{\tilde{u}_i \tilde{u}_j} + \overline{u_i' u_j'}, \tag{8}$$

where the second and third terms on the right-hand side represent the wave-induced and Reynolds stresses, respectively. The mean profiles of the wave-induced and Reynolds normal stresses are illustrated in Figs. 5 and 6 for the streamwise, vertical components, respectively. The shear stress is displayed in Fig. 7. The intensity of Reynolds stresses shown in Figs. 5(a), 6(a), and 7(a) are compared with the flat-wall case. The distributions of Reynolds stresses in the vertical direction for all wave cases are close to the flat-wall turbulence, only with less intensity for the streamwise component below $\bar{y}^+ \approx 50$. Meanwhile, the contributions of the wave-induced fluctuations provided in Figs. 5(b), 6(b), and 7(b) are significant, even greater than their turbulent counterparts. For the negative wave-age case ($c/U_b = -0.4$) and the stationary wavy wall case ($c/U_b = 0$), the

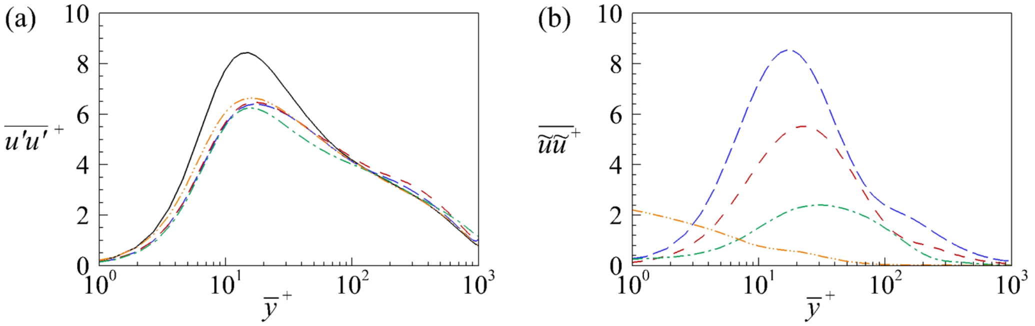

FIG. 5. Profiles of the streamwise velocity fluctuations for different wave ages as well as the flat-wall turbulence: (a) turbulent component; (b) wave-induced component. The definitions of the lines are the same as those in Fig. 4.

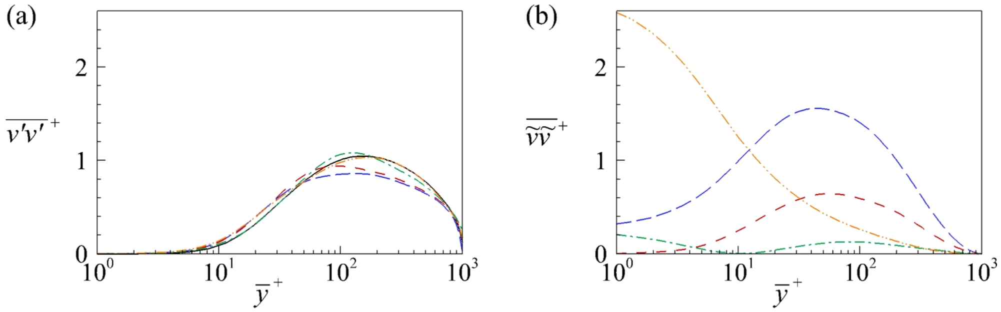

FIG. 6. Profiles of the vertical velocity fluctuations for different wave ages as well as the flat-wall turbulence: (a) turbulent component; (b) wave-induced component. The definitions of the lines are the same as those in Fig. 4.

wave-induced streamwise and vertical stresses achieve their peak values in the region of $\bar{y}^+ < 100$. Their correlation, the shear stress is negative in the near-wall region. As the wave age increases to $c/U_b = 0.4$ and 1.2, the location of the peak shifts upwards, while the amplitude decreases rapidly toward zero and then increases again. The variation of the peak with wave age reflects the influence of the critical layer [12]. In addition, for the positive wave-age cases, the wave-induced normal stresses near the wave surface increase due to the stronger orbital velocity at the wave surface [Eq. (5)]. Meanwhile, the wave-induced shear stress becomes positive below the critical layer.

To see more clearly, the phase averaged fields of the wave-induced streamwise and vertical velocity fluctuations near wave surface are presented in Figs. 8 and 9 for a whole wave period, and their correlation $-\tilde{u}\tilde{v}$ is shown in Fig. 10. The vertical displacement of the wave surface is enlarged for clearly displaying the wave phase. Note that the location of the critical layer is marked by the dashed line for $c/U_b = 0.4$ case. For $c/U_b = -0.4$ and 0, the critical layer does not exist, while for the fast wave case $c/U_b = 1.2$, the critical layer is far away from the boundary. The intensity and distribution of the wave-induced flow show strong dependence on both the wave phase and wave age. For $c/U_b = -0.4$ and 0, the streamwise and vertical components are positively correlated, i.e., both the $\tilde{u}$ and $\tilde{v}$ has the positive (negative) extrema in the windward (leeward) side due to the geometry and orbital velocity of wave surface [Figs. 8(a), 8(b), 9(a), and 9(b)]. Thus, their correlation $-\tilde{u}\tilde{v}$ is negative in these regions as seen in Figs. 10(a) and 10(b). When the wave age increases to $c/U_b = 0.4$ and 1.2, the $\tilde{u}$ contours are tilted upstream and the $\tilde{v}$ changes its sign below the critical layer [Figs. 8(c), 8(d), 9(c), and 9(d)]. Hence the original negative flux layer lifts further from the surface and a new layer with positive momentum flux is generated above the wave surface as shown in Figs. 10(c), 10(d), and 7(b). This phenomenon reveals that the critical layer can significantly alter

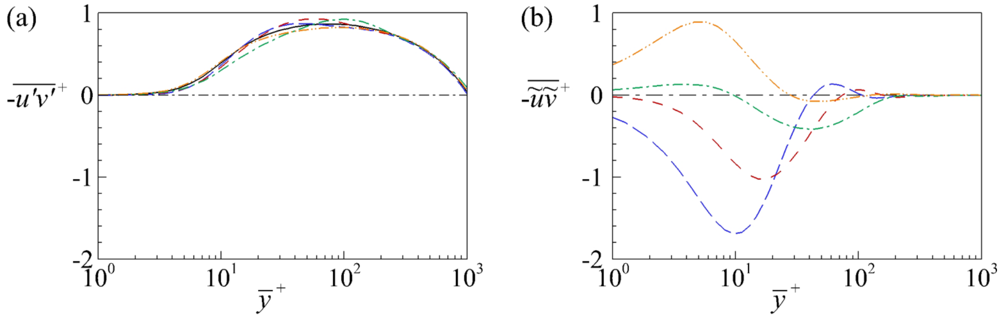

FIG. 7. Profiles of the shear stress for different wave ages as well as the flat-wall turbulence: (a) turbulent component; (b) wave-induced component. The definitions of the lines are the same as those in Fig. 4.

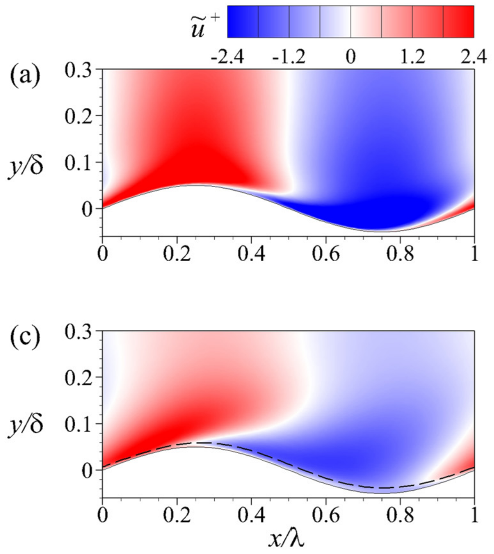

FIG. 8. Contours of the wave-induced streamwise velocity fluctuation: (a) $c/U_b = -0.4$; (b) $c/U_b = 0$; (c) $c/U_b = 0.4$; (d) $c/U_b = 1.2$.

the momentum flux transport in the vertical direction. Particular discussions on the wave-induced flow can be found in Sullivan *et al.* [12] using DNS, and in Buckley and Veron [30] using the laboratory experiment. The present flow patterns shown in Figs. 8 to 10 agree with their results.

Besides the wave-induced fluctuations, Yang and Shen [14,19] investigated the wave-phase-dependent modulation effect on the near-surface distribution of the Reynolds stresses. In their DNS results, these modulations are highly correlated with the orientation and location of coherent vortical structures in the near wall region [31]. The production term of the transport equation of Reynolds

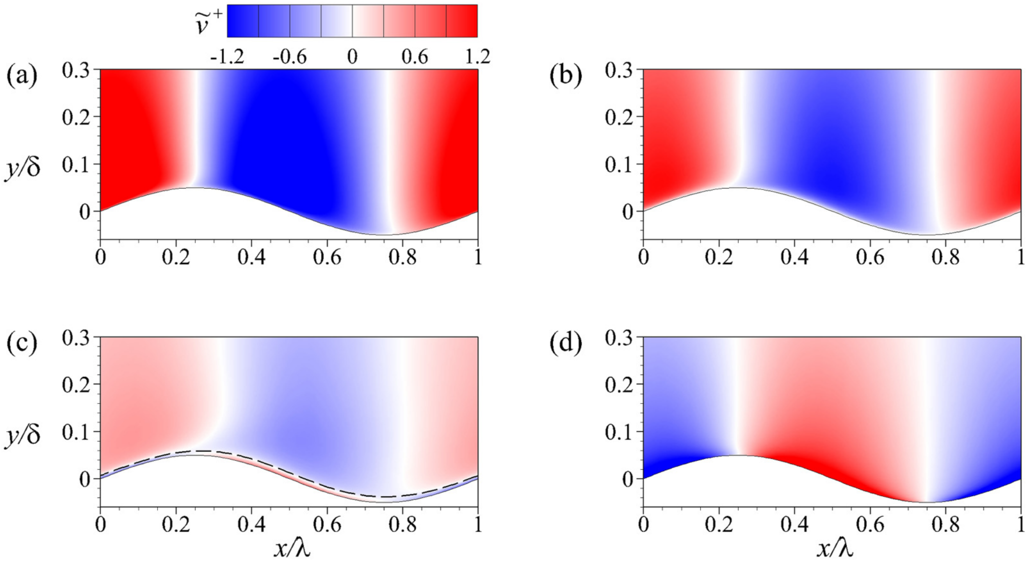

FIG. 9. Contours of the wave-induced vertical velocity fluctuation: (a) $c/U_b = -0.4$; (b) $c/U_b = 0$; (c) $c/U_b = 0.4$; (d) $c/U_b = 1.2$.

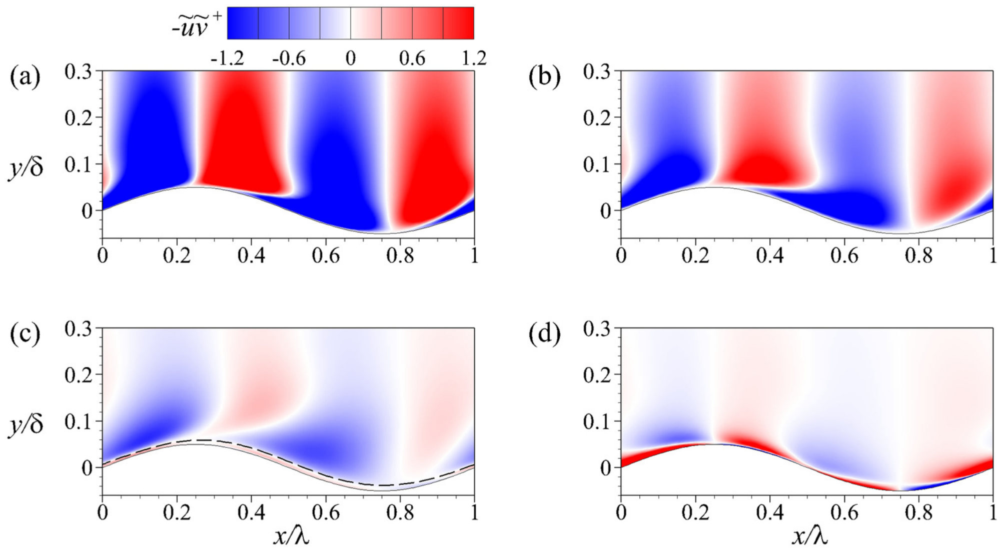

FIG. 10. Contours of the wave-induced shear stress: (a) $c/U_b = -0.4$; (b) $c/U_b = 0$; (c) $c/U_b = 0.4$; (d) $c/U_b = 1.2$.

stress directly reflects the interactions between the wave-induced flow and coherent structures. In the following, we mainly focus on the very large-scale motions in the outer layer. The transport equation of two-point correlation are used to investigate the interactions between the wave-induced flow and VLSMs, and these transport mechanisms affect the energy distribution among different scales of turbulent fluctuations, as will be discussed later.

B. Very large-scale turbulent motions

The instantaneous flow field in the streamwise-spanwise section at a certain vertical location is shown in Fig. 11 to visually describe the VLSMs. Contours of streamwise velocity fluctuation with blue and red regions represent the low- and high-speed regions, respectively. Figure 11(a) shows the fluctuation at $\bar{y}/\delta = 0.03(\bar{y}^+ \approx 30)$ for the flat-wall case. As several small-scale streamwise low-speed streaks are clearly visible in this inner region, these structures are classic coherent structures in the wall-bounded turbulence and scaled with the inner scale. Figure 11(f) shows the turbulent streamwise velocity fluctuations in the outer region $\bar{y}/\delta = 0.3(\bar{y}^+ \approx 300)$. In this region, the very large-scale streamwise elongated low- and high-speed streaks can be observed, which appear alternately in the spanwise direction and exhibits a meandering feature in the streamwise direction. Referring to the low-speed streaks in the inner region [Fig. 11(a)], a vague superposition effect can be observed, i.e., the faint footprints of the VLSMs in the outer region [Fig. 11(f)] appearing in the inner region [Fig. 11(a)]. This feature has also been described by Hutchins and Marusic [42] for the flat-wall turbulence and is considered as a type of the inner-outer interactions. The instantaneous flow patterns show a typical prospect of the turbulent VLSMs in the moderate and high Reynolds number turbulence reported in both the numerical and experimental studies, such as Hutchins and Marusic [39] and Lee and Sung [40]. Figures 11(b), 11(c), 11(g), and 11(h) show the instantaneous fields at the same vertical location for $c/U_b = -0.4$ and 0. The streaktype feature of the flow also widely exists in these cases, while the low- and high-speed VLSMs in the outer region [Figs. 11(g) and 11(h)] are more visible and coherent than the flat-wall turbulence. The spanwise length scale of these large-scale motions is also larger than the flat-wall case. There are three pairs of low- and high-speed streaks as can be clearly identified in Figs. 11(g) and 11(h) and the corresponding spanwise pseudoperiod is about $\lambda_z \approx 2\delta$. As shown in Figs. 11(b) and

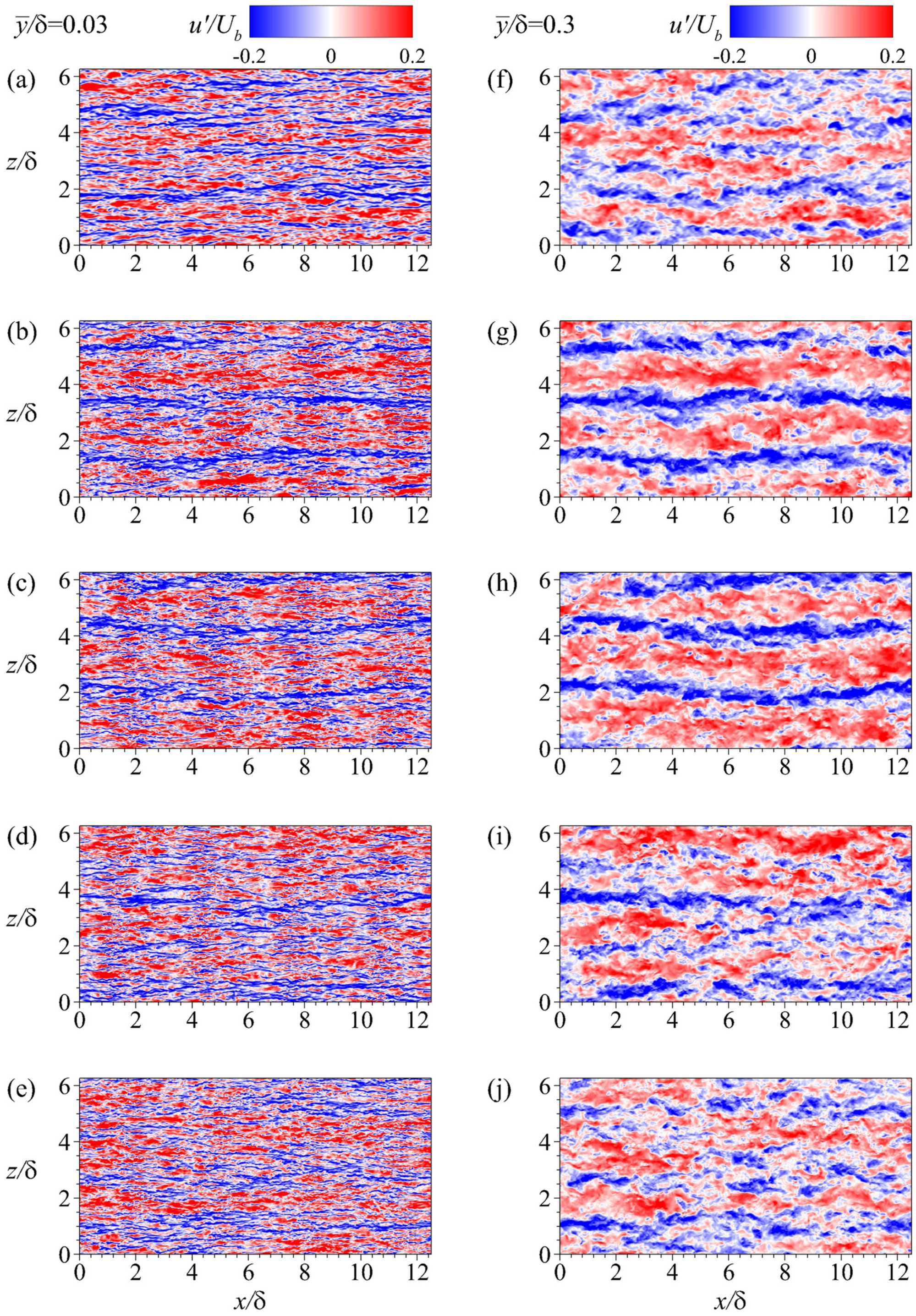

FIG. 11. Instantaneous turbulent streamwise velocity in the *x*-*z* plane: (a), (f) flat wall; (b), (g) $c/U_b = -0.4$; (c), (h) $c/U_b = 0$; (d), (i) $c/U_b = 0.4$; (e), (j) $c/U_b = 1.2$. Different vertical locations are chosen: (a)–(e) $\bar{y}/\delta = 0.03$; (f)–(j) $\bar{y}/\delta = 0.3$.

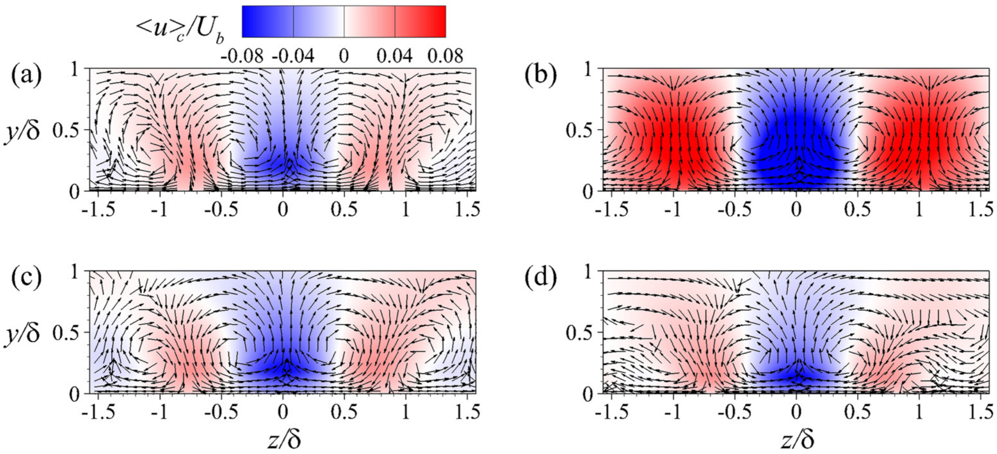

FIG. 12. Conditionally averaged streamwise velocity $\langle u \rangle_c$ and velocity vector in the y-z plane: (a) the flat-wall case; (b) $c/U_b = 0$; (c) $c/U_b = 0.4$; (d) $c/U_b = 1.2$.

11(c), the footprints from the low-speed VLSMs can be discerned more clearly in the inner region, accompanied by small-scale streaks. The instantaneous flow features indicate the stronger VLSMs and superposition effect in the wavy boundary turbulence. As the wave age increases to $c/U_b = 0.4$ and $c/U_b = 1.2$ [Figs. 11(d), 11(e), 11(i), and 11(j)], the spanwise length scale of the low-speed streaks is reduced and the flow pattern becomes similar to the flat-wall case. The similar large-scale pattern also can be obscurely observed in the instantaneous fields of v' and w' (not shown here).

To further investigate the physical mechanism on the formation of these VLSMs, the low-pass filter is used to extract the very large-scale turbulent fluctuation u'_L, and then a conditional average is implemented to gain the insight of the very large-scale coherent region. First, the turbulent streamwise velocity fluctuation is filtered by a truncated type low-pass filter in the spectral space. Based on the instantaneous fields and the energy spectra (will be discussed later) as shown in Figs. 11 and 13, the spanwise scale of the typical VLSMs is larger than the height of the open-channel δ. Thus, the chosen truncated wavelength is δ in the spanwise direction. Then the criterion $u'_L < 0$ is applied to discern the very large-scale low-speed events at the vertical location $\bar{y}/\delta = 0.1$. The spanwise-vertical sections of these conditionally averaged very large-scale low-speed events for the flat-wall case is shown in Fig. 12(a). The blue and red contours represent the conditionally averaged streamwise low- and high-speed regions, respectively. The low-speed region is flanked by high-speed regions on both sides and the quasi-period of the velocity variation is larger than δ but less than 2δ. The conditionally averaged transverse velocity illustrated by the superimposed vectors indicates that the very large-scale low- and high-speed regions are located between a pair of counter-rotating roll cells. The low-speed regions are induced by the large-scale ejecting events and the high-speed regions are accompanied by the motions sweeping toward the boundary. This behavior has been reported by amount of earlier works, such as Hutchins and Marusic [42] and Chung and McKeon [44]. Figure 12(b) shows the conditionally averaged field of the stationary wavy wall case. Note that the result of the $c/U_b = -0.4$ case is not included in Fig. 12 because it is similar with the $c/U_b = 0$ case. In general, the large-scale flow patterns in this case are similar to the flat-wall case. While the very large-scale streamwise velocity fluctuation is noticeably stronger and presents a more distinct periodicity in the spanwise direction. The distance between the two high-speed regions is slightly larger than 2δ, consistent with the instantaneous fields as seen in Figs. 11(g) and 11(h). Compared with the flat-wall turbulence, the roll cells between the low- and high-speed regions are also stronger and larger. Their influences extend from the bottom surface to the top of the open-channel and generate strong ejecting and sweeping motions in the vertical direction as well as converging and diverging motions in the spanwise direction. The similar conditionally averaged flow structures at the wave ages of $c/U_b = 0.4$ and $c/U_b = 1.2$ are displayed in Figs. 12(c) and 12(d). An obvious trend is that the length scale and intensity of the extracted VLSMs decrease with the increasing wave age.

Apparently, the length scale and intensity of the VLSMs are considerably affected by the wave surface. This trend is quantitatively confirmed by the energy spectra. One-dimensional pre-multiplied spanwise energy spectra of Reynolds stresses are shown in Fig. 13 for various wave ages together with the flat-wall case. Here, the spectral densities shown in the logarithmic plot have been pre-multiplied by the spanwise wave number k_z to show the integral contribution per $\log k_z$. Figure 13(i) shows the energy spectra of the flat-wall turbulence. Two peaks can be observed in the spectra of the streamwise velocity [Fig. 13(i-a)] and shear stress [Fig. 13(i-d)] that correspond to the inner/outer scale separation [58,65–67] in high Reynolds number turbulence. The inner peak locates at the scale around $\lambda_z^+ \approx 130$, which corresponds to the near-wall velocity streaks. The outer peak locates at the scale around $\lambda_z/\delta \approx 1.57$, which represents the turbulent VLSMs in the outer region. The scale of the outer peak shown in Fig. 13(i-a) is similar with the channel flows, i.e., $\lambda_z \approx 1.2 \sim 1.6\delta$ [58,68,69], while larger than those in the boundary layers, i.e., $\lambda_z \approx 0.8\delta$ [66,67]. It is known that the spanwise length scale of the VLSMs reported in turbulent channel flow is larger than those reported in turbulent boundary layers [42,70]. Note that the very large-scale peak region expanding from the outer region to the inner region indicates the superposition effect of the VLSMs on the inner region [42,43].

Although the mean profiles of Reynolds stresses for wavy boundary turbulence shown in Figs. 5–7 have the similar intensities and vertical distributions with the flat-wall case, distinct differences appear in their energy spectra. For $c/U_b = -0.4$ [Fig. 13(ii-a)] and $c/U_b = 0$ [Fig. 13(iii-a)], the outer peak located at a larger scale around $\lambda_z/\delta \approx 2.11$ is more vivid and extends more deeply into the inner region. As the wave age increases to $c/U_b = 0.4$, the scale of the outer peak [Fig. 13(iv-a)] reduces back to $\lambda_z/\delta \approx 1.57$ and the amplitude also decreases. For $c/U_b = 1.2$ [Fig. 13(v-a)], the large-scale peak decreases further and the spectra is similar with the flat-wall case. Noteworthily, Lee [58] reported the spectra of turbulent channel flow obtained from DNS data at the Reynolds numbers of $\mathrm{Re}_\tau = 1000$ and $\mathrm{Re}_\tau = 5200$. He mentioned that at the relatively low Reynolds number, i.e., $\mathrm{Re}_\tau = 1000$, the separation of scales can only be observed in the streamwise velocity. Interestingly, in our wavy boundary cases, the separation of length scale can also be observed in the vertical and spanwise velocities. For the vertical velocity fluctuation [Fig. 13(b)], the flat-wall turbulence [Fig. 13(i-b)] achieves its peak value only at a relatively small scale. While for $c/U_b = -0.4$ [Fig. 13(ii-b)] and $c/U_b = 0$ [Fig. 13(iii-b)], an additional very large-scale peak can be observed. The scale of the second peak is the same as the streamwise velocity. For the spanwise component [Fig. 13(c)], the additional very large-scale peak can even be seen in the $c/U_b = 0.4$ case. The scale separation of the turbulent vertical and spanwise velocities can be explained by the enhanced very large-scale transverse flow as depicted in Fig. 12(b).

In our results, the very large-scale peaks of all the velocity components occur at the same scale (marked by the dash-dot line in Fig. 13) for each wave age but in different vertical regions, namely $\bar{y}/\delta \approx 0.5$ for the vertical velocity, $\bar{y}/\delta \approx 0.08$ for the spanwise velocity. The very large-scale peak of streamwise velocity exists in both inner- and outer-regions and centered at $\bar{y}/\delta \approx 0.3$. Then we examine the spectra of all the velocity components at these locations (marked by the dashed line in Fig. 13) and use the corresponding mean energy of velocity fluctuation at the same vertical location to normalize the spectra, i.e.,

$$E^n_{u_i'u_j'}(k, \bar{y}) = E_{u_i'u_j'}(k, \bar{y}) / \overline{u_i'u_j'}(\bar{y}). \tag{9}$$

After normalization, the integral of spectral density over the wave number is unit for all the cases. Figure 14(a) shows the energy spectra of turbulent streamwise velocity fluctuation in the inner region $\bar{y}/\delta = 0.03$ ($\bar{y}^+ \approx 30$). In general, the streamwise turbulent velocity fluctuation is mainly concentrated in small scales and the very large-scale peak is relatively weak. While more energy distributes in large scales for the wavy boundary cases, their small-scale energy is slightly reduced, correspondingly. Figure 14(b) shows the spectra at a higher vertical location $\bar{y}/\delta = 0.3$ ($\bar{y}^+ \approx 300$).

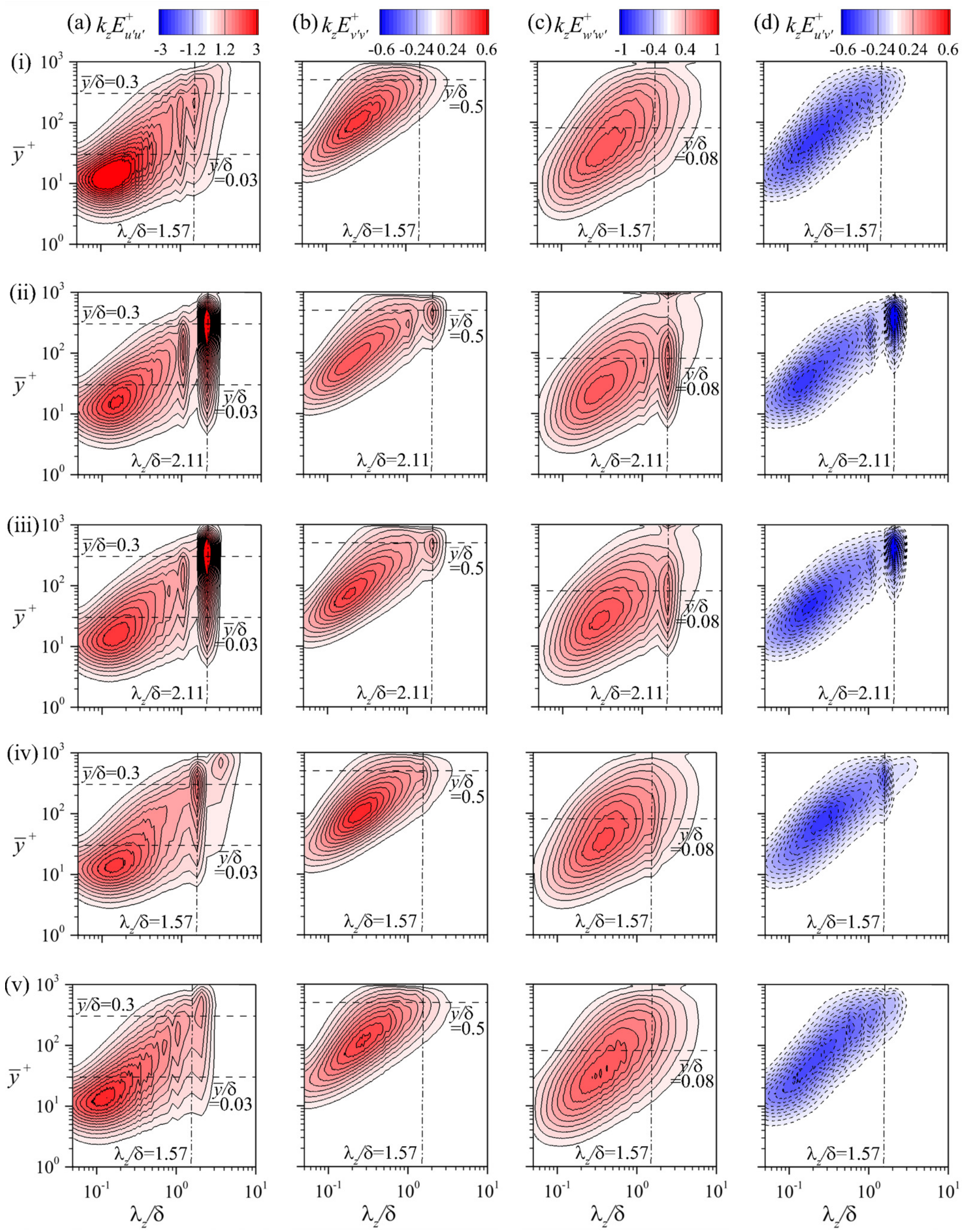

FIG. 13. Contours of the one-dimensional pre-multiplied spanwise energy spectra of turbulent velocity fluctuations: (i) the flat-wall case; (ii) $c/U_b = -0.4$; (iii) $c/U_b = 0$; (iv) $c/U_b = 0.4$; (v) $c/U_b = 1.2$. Different components, i.e., (a) $\overline{u'u'}$, (b) $\overline{v'v'}$, (c) $\overline{w'w'}$, and (d) $\overline{u'v'}$ are presented.

In this outer region, the turbulent energy is mainly concentrated at large scales. A sharper and stronger peak at the scale of $\lambda_z/\delta \approx 2.11$ can be observed in $c/U_b = -0.4$ and $c/U_b = 0$ cases. When the wave age increases to $c/U_b = 0.4$, the scale of the peak reduces back to $\lambda_z/\delta \approx 1.57$ as in

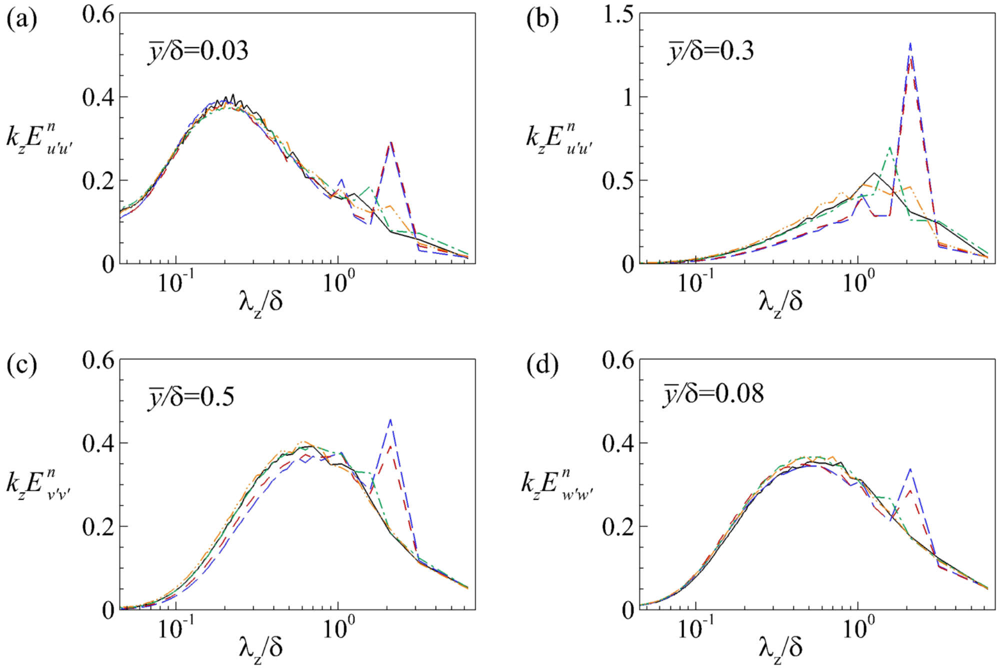

FIG. 14. Normalized one-dimensional premultiplied spanwise energy spectra of turbulent velocity fluctuations for various wave ages at different vertical locations: (a) streamwise component $u', \bar{y}/\delta = 0.03$; (b) streamwise component $u', \bar{y}/\delta = 0.3$; (c) vertical component $v', \bar{y}/\delta = 0.5$; (d) spanwise component $w', \bar{y}/\delta = 0.08$. The different lines represent the different wave ages, the same as those in Fig. 4.

the flat-wall case but still with a stronger intensity. The spectra of vertical and spanwise velocities at two different locations are shown in Figs. 14(c) and 14(d), respectively. For the flat-wall turbulence, the energy distributes in a relatively wide range of scales and only a gentle peak exists. While for the $c/U_b = -0.4$ and 0 cases, there is an additional sharp peak existing at a very large scale. Meanwhile, the energy distributed in small scales ($\lambda_z/\delta < 1$) for the vertical velocity is reduced as compared with the flat-wall turbulence. As the wave age increases to $c/U_b = 0.4$, the scale and intensity of the very large-scale peak are reduced sharply. For the $c/U_b = 1.2$ case, the spectra for all the components nearly coincides with the flat-wall turbulence. In general, both the length scale and amplitude of the very large-scale peak decrease as the wave age increases.

It is noted that the above VLSMs scaling with $1.57 \sim 2.11\delta$ (δ is the height of the open-channel) in the wavy boundary cases are similar to the previous experimental work on the stationary wavy boundary layer flow [50], where velocity streaks and vortex pairs are scaled with the boundary layer thickness. In the experiments of the stationary wavy-wall channel flow [51–53], the large-scale flow motion extracted by the first two eigenmodes of POD has a scale of $1 \sim 1.5$ times of the full channel height in the spanwise direction, which is $2 \sim 3\delta$ and larger than our results. While the radius of the corresponding counter-rotating vortices detected by the eigenfunctions is about 0.5 times of the full channel height, which is similar with our conditional averaged flow fields as shown in Fig. 12. Considering their wave amplitude ($a/\delta = 0.1$ and 0.2) and steepness ($ak_w = 0.1\pi$ and 0.2π) [53] is much larger than ours, i.e., $a/\delta = 0.05$ and $ak_w = 0.1$ (Table I), the discrepancy in length scale might be due to the different wave parameters. The effect of the wave steepness will be discussed later.

Moreover, the spanwise length scale of VLSMs varies from $\lambda_z/\delta \approx 1.57$ to $\lambda_z/\delta \approx 2.11$ for different cases. Considering the computational domain size in the spanwise direction $L_z = 2\pi\delta$, the above length scales correspond to four pseudo-periods in domain for the flat-wall, $c/U_b = 0.4$

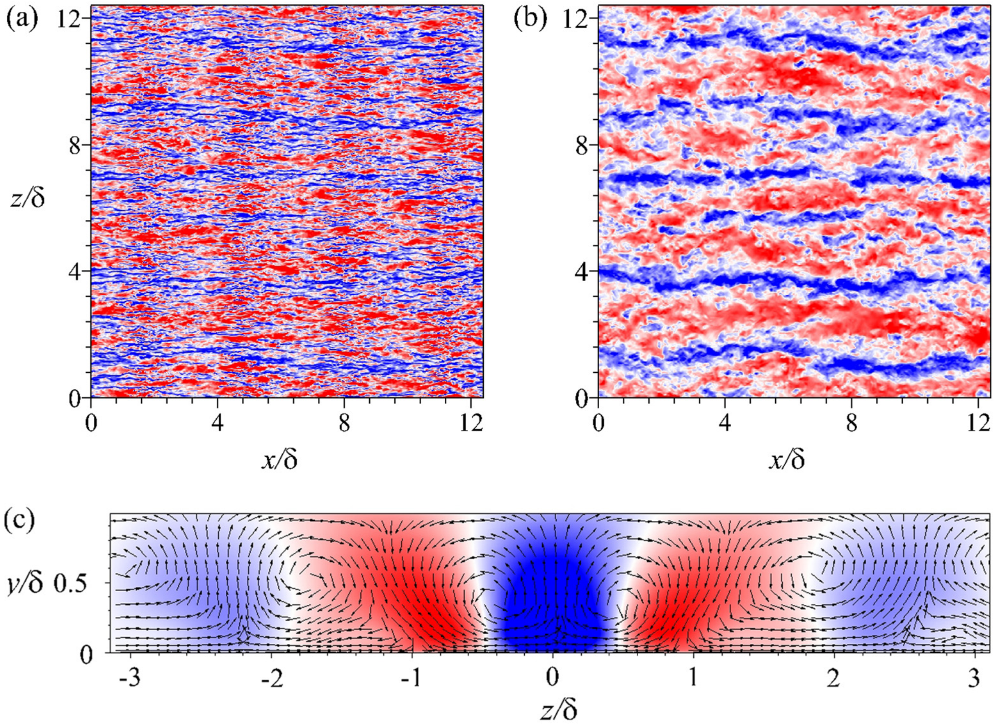

FIG. 15. Instantaneous turbulent streamwise velocity in the *x*-*z* plane: (a) $\bar{y}/\delta = 0.03$; (b) $\bar{y}/\delta = 0.3$; the contours are same as those in Fig. 11. (c) Conditionally averaged streamwise velocity and velocity vector in the *y*-*z* plane; the contours are same as those in Fig. 12.

and $c/U_b = 1.2$ cases, while three pseudoperiods for the $c/U_b = -0.4$ and $c/U_b = 0$ cases. Thus, we check the influence of the computational domain size on the length scale of VLSMs. Here a larger domain with doubled size in the spanwise direction ($L_z = 4\pi\delta$) is tested for the stationary wavy wall case. Similarly, the VLSMs extracted from the instantaneous and conditionally averaged flow fields shown in Fig. 15 are much stronger than those in the flat-wall case. As seen in Fig. 15(b), several very large-scale low-speed streaks exist in the instantaneous flow field. The instantaneous flow pattern is similar with the smaller domain case [Fig. 11(h)]. While the distance between the conditional sampled streaks quantitatively shown in Fig. 15(c) is slightly larger than that extracted from the smaller domain case [Fig. 12(b)]. Although the specific size of the VLSMs is slightly affected by the domain size, the formation of VLSMs is the same for all the cases and the trend is clear that the VLSMs are enhanced and enlarged by the wavy boundary. The underlying mechanism will be discussed later.

C. Spectral analysis on the transport equation of two-point velocity correlation

To reveal the mechanism of the enhanced turbulent VLSMs in the wavy boundary cases, the transport equation of the two-point velocity correlation function is analyzed, as in Lee [58] and Lee and Moser [71,72], which can be expressed as

$$\overline{\frac{\partial u_i' u_{rj}'}{\partial t}} + \langle u_k \rangle \overline{\frac{\partial \langle u_i' u_{rj}' \rangle}{\partial x_k}} = P_{ij} + \Pi_{s,ij} + \Pi_{t,ij} + D_{ij} + T_{ij} - \varepsilon_{ij} + WP_{ij}; \tag{10}$$

$$P_{ij} = -\overline{u_{jr}' v'}\,\overline{\frac{\partial u_i}{\partial y}} - \overline{u_i' v_r'}\,\overline{\frac{\partial u_j}{\partial y}} - \overline{u_{jr}' u'}\,\overline{\frac{\partial u_i}{\partial x}} - \overline{u_i' u_r'}\,\overline{\frac{\partial u_j}{\partial x}}; \tag{11}$$

$$\Pi_{s,ij} = \overline{p'\frac{\partial u'_{jr}}{\partial x}}\delta_{i1} + \overline{p'_r\frac{\partial u'_i}{\partial x}}\delta_{j1} + \overline{p'\frac{\partial u'_{jr}}{\partial y}}\delta_{i2} + \overline{p'_r\frac{\partial u'_i}{\partial y}}\delta_{j2} + \frac{\partial \overline{p'u'_{jr}}}{\partial r_z}\delta_{i3} - \frac{\partial \overline{p'_r u'_i}}{\partial r_z}\delta_{j3}; \tag{12}$$

$$\Pi_{t,ij} = -\frac{\partial \overline{p'u'_{jr}}}{\partial x}\delta_{i1} - \frac{\partial \overline{p'_r u'_i}}{\partial x}\delta_{j1} - \frac{\partial \overline{p'u'_{jr}}}{\partial y}\delta_{i2} - \frac{\partial \overline{p'_r u'_i}}{\partial y}\delta_{j2}; \tag{13}$$

$$D_{ij} = \frac{1}{\mathrm{Re}}\frac{\partial^2 \overline{u'_i u'_{jr}}}{\partial x^2} + \frac{1}{\mathrm{Re}}\frac{\partial^2 \overline{u'_i u'_{jr}}}{\partial y^2}; \tag{14}$$

$$\begin{aligned} T_{ij} = {} & -\frac{\partial \overline{u'_{jr}(u'_i u')}}{\partial x} - \frac{\partial \overline{u'_i (u'_j u')_r}}{\partial x} - \frac{\partial \overline{u'_{jr}(u'_i v')}}{\partial y} - \frac{\partial \overline{u'_i (u'_j v')_r}}{\partial y} \\ & + \overline{u'_i u' \frac{\partial u'_{jr}}{\partial x}} + \overline{u'_i v' \frac{\partial u'_{jr}}{\partial y}} + \overline{(u'_j u')_r \frac{\partial u'_i}{\partial x}} + \overline{(u'_j v')_r \frac{\partial u'_i}{\partial y}} \\ & + \frac{\partial \overline{u'_{jr}(u'_i w')}}{\partial r_z} - \frac{\partial \overline{u'_i (u'_j w')_r}}{\partial r_z} + T_{\mathrm{SGS},ij}; \end{aligned} \tag{15}$$

$$\varepsilon_{ij} = \frac{2}{\mathrm{Re}}\overline{\frac{\partial u'_i}{\partial x}\frac{\partial u'_{jr}}{\partial x}} + \frac{2}{\mathrm{Re}}\overline{\frac{\partial u'_i}{\partial y}\frac{\partial u'_{jr}}{\partial y}} + \frac{2}{\mathrm{Re}}\frac{\partial^2 \overline{u'_i u'_{jr}}}{\partial r_z^2} + \varepsilon_{\mathrm{SGS},ij}. \tag{16}$$

Here P_{ij}, $\Pi_{s,ij}$, $\Pi_{t,ij}$, D_{ij}, T_{ij}, and ε_{ij} denote the production, pressure-strain, pressure diffusion, viscous diffusion, turbulent diffusion, and dissipation terms, respectively. The subscript "r" represents the quantity at the location with a certain distance in the spanwise direction from the reference point. A brief introduction to the derivation of the above transport equation and its spectral expression can be found in Appendix B. Similar equations for the flat-wall turbulence can be referred to in Lee [58] but without $T_{\mathrm{SGS},ij}$ and $\varepsilon_{\mathrm{SGS},ij}$, which represent the transport and dissipation terms induced by the SGS stress, respectively. Different with their derivation process, we replace the classic Reynolds decomposition with the triple decomposition according to Eq. (7). As a result, the additional term, which is referred to as the wave-induced production term, appears at the right-hand side of Eq. (10), i.e.,

$$\begin{aligned} WP_{ij} &= -\overline{\langle u'_{jr}v'\rangle\left\langle\frac{\partial u_i}{\partial y}\right\rangle} - \overline{\langle u'_i v'_r\rangle\left\langle\frac{\partial u_j}{\partial y}\right\rangle} - \overline{\langle u'_i u'_r\rangle\left\langle\frac{\partial u_j}{\partial x}\right\rangle} - \overline{\langle u'_{jr}u'\rangle\left\langle\frac{\partial u_i}{\partial x}\right\rangle} - P_{ij} \\ &= -\overline{\widetilde{u'_{jr}v'}\frac{\widetilde{\partial u_i}}{\partial y}} - \overline{\widetilde{u'_i v'_r}\frac{\widetilde{\partial u_j}}{\partial y}} - \overline{\widetilde{u'_{jr}u'}\frac{\widetilde{\partial u_i}}{\partial x}} - \overline{\widetilde{u'_i u'_r}\frac{\widetilde{\partial u_j}}{\partial x}}, \end{aligned} \tag{17}$$

where the tilde terms represent the wave-induced variations in the streamwise direction. The wave-induced production term WP_{ij} [Eq. (17)] consists the product of the wave-induced Reynolds stresses and velocity gradients, and thus only exists in the wavy boundary cases. For the flat-wall case, WP_{ij} should be zero. Since Eqs. (10)–(17) are obtained by averaging in time, streamwise and spanwise direction, all the terms are functions of the spanwise separation distance r_z and the mean vertical location $\bar{y}$. Note that according to the definition given in Appendix B, the mean and triple decomposition operators cannot interchange with the spatial derivatives. Rewriting the equations in a curvilinear coordinate system will present every term in a simpler way, i.e., that all the mean and wave-induced components in Eqs. (10)–(17) can be moved inside the derivatives. Thus, through the operators defined in Appendix B, the wave-induced production [Eq. (17)] can be separated from the whole production. When the spanwise separation length is zero, i.e., $r_z = 0$, Eq. (10) is approximately degenerated to the classic transport equation of the Reynolds stresses, which had been studied for the wavy boundary turbulence to describe the mechanism of momentum transport in the vertical direction [57] and the Reynolds stresses generation in different wave phases [14,31].

As pointed out by Reynolds and Hussain [12], the wave-induced production term WP_{ij} represents the energy exchange between the Reynolds stresses $\overline{u'_i u'_j}$ and the wave-induced stresses $\overline{\tilde{u}_i \tilde{u}_j}$.

In the present work, the spanwise length scale is allowed to vary in Eq. (10), and the spectral analysis is implemented as defined in Appendix B to reveal the contribution of each term in different length scales. The whole spectral analysis for the transport equation of the two-point velocity correlation function in turbulent Poiseuille and Couette flows had been studied at a range of Reynolds numbers by Lee [58] and Lee and Moser [72]. In general, the energy transfer process in the flat-wall turbulence can be described briefly as follows: the production term generates the small-scale (large-scale) turbulent kinetic energy (TKE) in the inner (outer) region; the synthetic contributions of the pressure diffusion, viscous diffusion and turbulent diffusion terms are transferring the energy among the different length scales and along the vertical direction; the TKE is dissipated mainly in small scales in both the inner and outer regions; the pressure-strain term transfers the energy among the three velocity components.

In our results, the spectra of these terms for the flat-wall case conform to Lee [58], and they are generally similar in the wavy boundary cases. In this section, we focus on the spectra of the terms dominating the energy gain of Reynolds stresses and momentum flux, i.e., production terms for $\overline{u'u'}$ and $\overline{u'v'}$, and pressure-strain terms for $\overline{v'v'}$ and $\overline{w'w'}$, respectively. In the following, the spectral densities shown in the logarithmic plot are pre-multiplied by k_z and $\bar{y}^+$ to represent their integral contributions. As shown in Fig. 16(a), according to $E_{P11} = -E_{uv}\overline{\partial u/\partial y}$, the spectral of the production term of $\overline{u'u'}$ for all the cases is similar to the corresponding spectra of $\overline{u'v'}$ as seen in Fig. 13(d). The production term has two peaks, with the inner peak located at the scale $\lambda_z/\delta \approx 0.15$ and the outer peak occurring at $\lambda_z/\delta = 1.57$ or 2.11. The variation of the spectra with the wave age is also similar with that of $\overline{u'v'}$. For $c/U_b = -0.4$ [Fig. 16(ii-a)] and $c/U_b = 0$ [Fig. 16(iii-a)], both the intensity and scale of the outer peaks are increased as compared with the flat-wall turbulence. When the wave age increases to $c/U_b = 0.4$, the outer peak is weakened and their length scale is reduced [Fig. 16(iv-a)]. The outer peak is almost disappeared for case $c/U_b = 1.2$. The spectra of the production term for the Reynolds shear stress, P_{12}, in Fig. 16(d) has also a similar pattern with that of $\overline{v'v'}$ as shown in Fig. 13(b), according to $E_{P12} = -E_{vv}\overline{\partial u/\partial y}$. For $c/U_b = -0.4$ [Fig. 16(ii-d)] and $c/U_b = 0$ [Fig. 16(iii-d)], an additional very large-scale peak can be observed. There is no production term in the transport equations of the vertical and spanwise components, which gain energy from the streamwise component by the pressure-strain term as shown in Figs. 16(b) and 16(c). For the flat-wall turbulence, the pressure-strain term transfers the energy from $\overline{v'v'}$ to the other two components [blue region in Fig. 16(i-b)] within the region $\bar{y}^+ < 10$, and above that, the energy is transferred to $\overline{v'v'}$. For $c/U_b = -0.4$ [Fig. 16(ii-b)] and $c/U_b = 0$ [Fig. 16(iii-b)], the region losing energy extends to a higher vertical location and a very large-scale peak with energy gain occurs in the outer region. The outer peaks disappear as the wave age increases [Figs. 16(iv-b) and 16(v-b)]. The spectra of the spanwise component [Fig. 16(c)] has a weaker wave age dependence as compared with the other components, while an indistinct peak in the outer region can still be distinguished in the $c/U_b = -0.4$ and 0 cases [Figs. 16(ii-c) and 16(iii-c)].

For all the wavy boundary cases, the wave-induced production term WP_{ij} provides an additional mechanism of energy gain or loss. For the streamwise and vertical turbulent velocity fluctuations and the Reynolds shear stress, the wave-induced production terms can be further expressed as

$$WP_{11} = -\overline{(\widetilde{u'_r v'} + \widetilde{u'v'_r})\frac{\partial \tilde{u}}{\partial y}} - 2\overline{\widetilde{u'u'_r}\frac{\partial \tilde{u}}{\partial x}} = WP_{11,uy} + WP_{11,ux}, \tag{18}$$

$$WP_{22} = -2\overline{\widetilde{v'v'_r}\frac{\partial \tilde{v}}{\partial y}} - \overline{(\widetilde{u'_r v'} + \widetilde{u'v'_r})\frac{\partial \tilde{v}}{\partial x}} = WP_{22,vy} + WP_{22,vx}, \tag{19}$$

$$\begin{aligned} WP_{12} &= -\overline{\widetilde{v'v'_r}\frac{\partial \tilde{u}}{\partial y}} - \overline{\widetilde{u'v'_r}\frac{\partial \tilde{v}}{\partial y}} - \overline{\widetilde{u'v'_r}\frac{\partial \tilde{u}}{\partial x}} - \overline{\widetilde{u'u'_r}\frac{\partial \tilde{v}}{\partial x}} \\ &= WP_{12,uy} + WP_{12,vy} + WP_{12,ux} + WP_{12,vx}. \end{aligned} \tag{20}$$

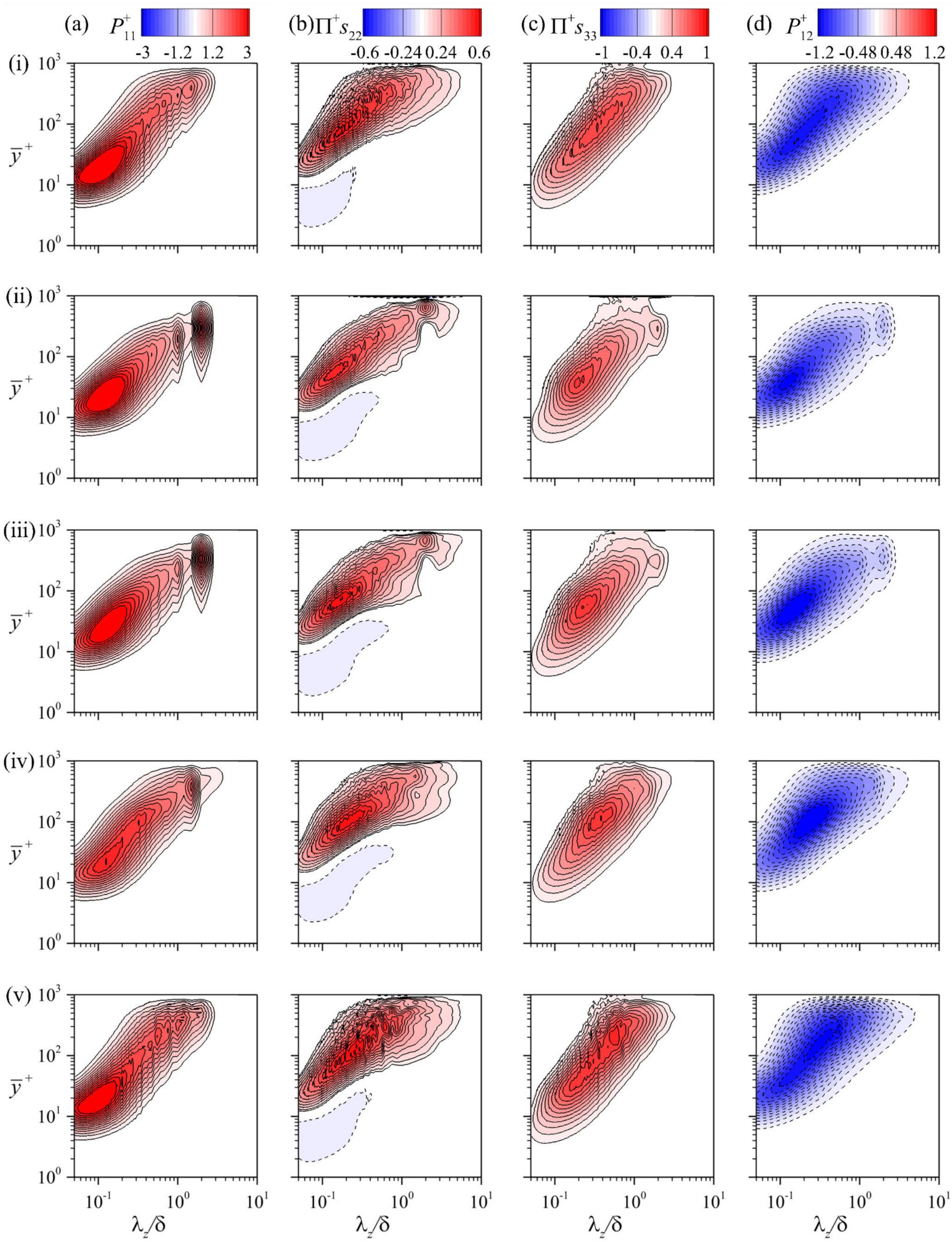

FIG. 16. Contours of the one-dimensional pre-multiplied spanwise energy spectra of the production and pressure-strain terms: (i) the flat-wall case; (ii) $c/U_b = -0.4$; (iii) $c/U_b = 0$; (iv) $c/U_b = 0.4$; and (v) $c/U_b = 1.2$. Different terms, i.e., (a) P_{11}, (b) Π_{s22}, (c) Π_{s33}, and (d) P_{12} are presented.

Note that in the above expressions, both the turbulent two-point correlation function $(\widetilde{u'_i u'_j})$ and the velocity gradient $(\widetilde{\partial u_i/\partial x_j})$ are varied in the streamwise direction for different wave phases and the wave-induced production WP_{ij} is generated by their correlation within the whole wave period.

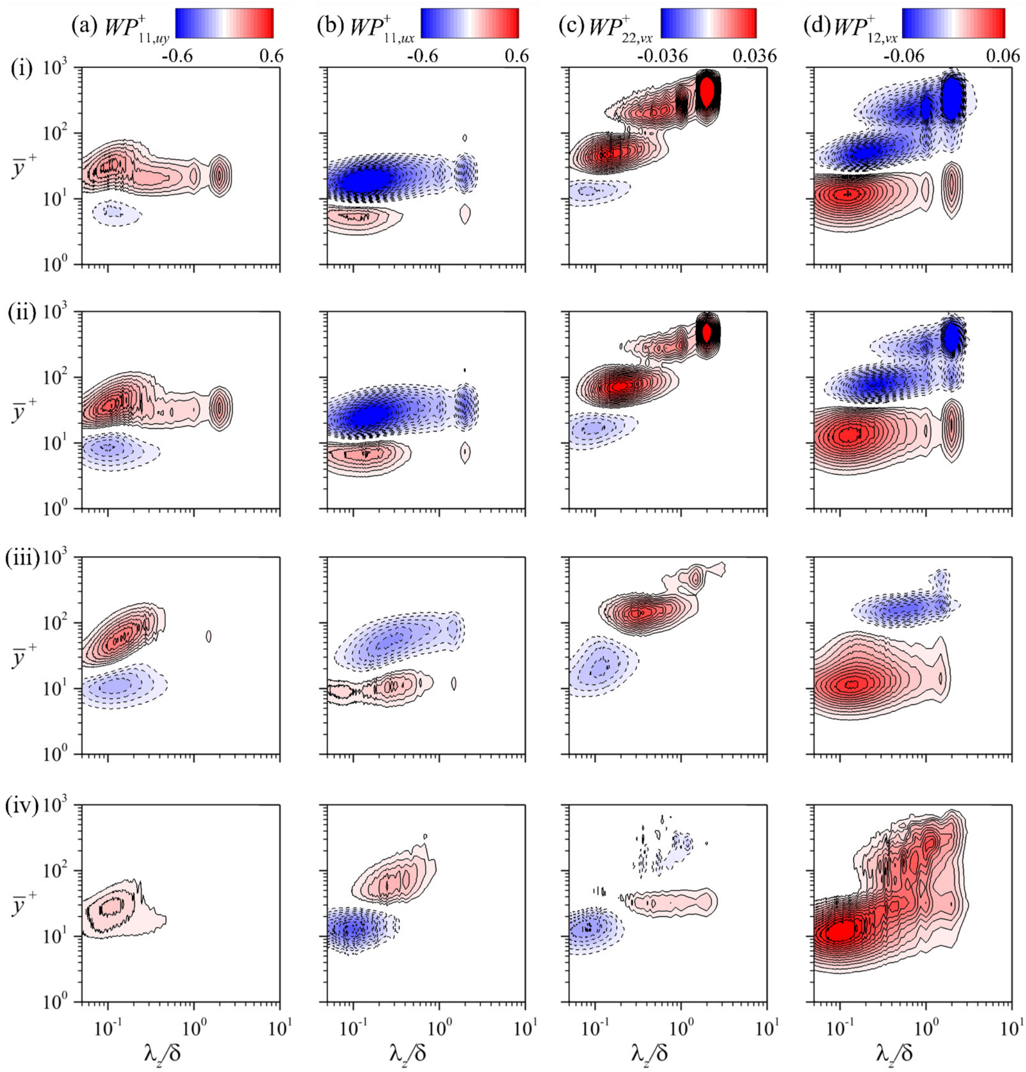

FIG. 17. Contours of the one-dimensional pre-multiplied spanwise energy spectra of wave-induced production terms for different wave-ages: (i) $c/U_b = -0.4$; (ii) $c/U_b = 0$; (iii) $c/U_b = 0.4$; (iv) $c/U_b = 1.2$. Different terms, i.e., (a) $WP_{11,uy}$, (b) $WP_{11,ux}$, (c) $WP_{22,vx}$, and (d) $WP_{12,vy}$ are presented.

For the streamwise velocity fluctuation, both terms on the right-hand side of Eq. (18) are important. The one-dimensional spectra of the first term, $WP_{11,uy}$, for various wave ages are plotted in Fig. 17(a), which can be divided into two regions in the vertical direction with different signs. For $c/U_b = -0.4$ [Fig. 17(i-a)], $WP_{11,uy}$ has positive contribution to both small and large scales in the region $\bar{y}^+ > 10$. The bimodal characteristics indicate that the turbulent fluctuation gains energy from this term in both small and large scales. As the wave age increases, the positive region loses its peak in the large scale and becomes weak in the $c/U_b = 0.4$ case [Fig. 17(iii-a)] and a considerable negative contribution to the small scale occurs in the region $\bar{y}^+ \approx 10$. For the fast wave case $c/U_b = 1.2$ [Fig. 17(iv-a)], this term has only a positive small-scale peak in the region of $10 < \bar{y}^+ < 100$. Figure 17(b) shows the spectra of the second term on the right-hand side of Eq. (18). For $c/U_b = -0.4$, 0, and 0.4, $WP_{11,ux}$ has also two regions on either side of $\bar{y}^+ \approx 10$. Its effect is nearly opposite to $WP_{11,uy}$ and also becomes weak as the wave age increases. Interestingly, the regions exchange their signs in the fast-wave case $c/U_b = 1.2$ [Fig. 17(iv-a)].

For the turbulent vertical velocity fluctuation, the second term on the right-hand side of Eq. (19), $WP_{22,vx}$, is the dominant term in the wave-induced production. Figure 17(i-c) shows the spectra of $WP_{22,vx}$ for $c/U_b = -0.4$, where three regions can be identified. The first one locates at $\bar{y}^+ < 30$ which belongs to the buffer layer. $WP_{22,vx}$ has negative contribution to the small-scale fluctuation in this region. As the wave age increases from negative to positive, this small-scale energy loss region enlarges and lifts a little in the vertical direction. The second region locates between $\bar{y}^+ > 30$ and $\bar{y}^+ < 300$. According to the Reynolds number in our simulations, i.e., $\mathrm{Re}_\tau \approx 1000$, this region belongs to the logarithmic region. $WP_{22,vx}$ has positive contribution to the small-scale fluctuation for $c/U_b = -0.4$ [Fig. 17(i-c)]. This energy gain region lifts up in the vertical direction with the increasing wave age but becomes weak and shifts to the large scale [Fig. 17(iv-c)]. The third region in the spectra of $WP_{22,vx}$ is in the outer layer, from $\bar{y}^+ > 200$ upon to the top of the open channel. For $c/U_b = -0.4$, a distinct positive peak occurs at $\bar{y}/\delta \approx 0.5$ ($\bar{y}^+ \approx 500$). As the wave age increases, the amplitude and length scale of this very large-scale peak are decreased and even becomes negative in the fast wave case $c/U_b = 1.2$ [Fig. 17(iv-c)]. Comparing with Fig. 14(c), we can see that the length scale, the vertical location and the variation trend of the spectra of $WP_{22,vx}$ are consistent with those of the turbulent vertical velocity fluctuation. The similar spectra characteristics indicate that $WP_{22,vx}$ has an important effect on the very large-scale vertical velocity fluctuation.

The dominant term of the wave-induced production for the Reynolds shear stress is the last term at the right-hand side of Eq. (20), $WP_{12,vx}$, and its spectra for various wave ages are shown in Fig. 17(d). Note that because of the turbulent momentum flux $\overline{u'v'}$ is usually negative, the blue region in Fig. 17(d) represents the energy gain and the red region is the energy loss region. The spectral feature of $WP_{12,vx}$ is similar with $WP_{22,vx}$, where three regions can be distinguished. For $c/U_b = -0.4$ [Fig. 17(i-d)], both the large- and small-scale momentum fluxes lose energy in the buffer layer ($\bar{y}^+ < 30$) and gain energy in the logarithmic region. The very large-scale flux in the outer layer has strong energy input due to this term. When the wave age increases, a wide range of scales loses more energy in the buffer layer, and meanwhile, their energy input in the logarithmic region and outer layer is decreased and then becomes negative at $c/U_b = 1.2$ [Fig. 17(iv-d)].

In summary, the one-dimensional spectra of the budget terms shown in Figs. 16 and 17 inherit the characteristics of turbulent fluctuations in the outer region. In the flat-wall turbulence, the vertical velocity fluctuation $\overline{v'v'}$ has no production term in its transport equation ($P_{22} = 0$) and can only receive energy from $\overline{u'u'}$ through the pressure-strain term. While in the low wave-age situations, the very large-scale $\overline{v'v'}$ can be generated by $WP_{22,vx}$ which is induced by the interaction between very large-scale $-\widetilde{u'v'}$ and $\widetilde{\partial v/\partial x}$. The Reynolds shear stress $-\overline{u'v'}$ can also gain extra very large-scale energy from $WP_{12,vx}$. Both of these two terms decrease as the wave age increases and becomes negative at $c/U_b = 1.2$, which indicates that the wave-induced fluctuation gains energy from the very large-scale $\overline{v'v'}$ and $-\overline{u'v'}$. Although there is no wave-induced production term in the transport equation of the spanwise velocity fluctuation ($WP_{33} = 0$), the very large-scale spanwise motion gains energy from $\overline{u'u'}$ by the pressure-strain term as shown in Fig. 16(c). The budget analysis supports that the wave-induced production provides an additional mechanism of gaining or losing very large-scale energy from the mean flow, which is perturbed by the wavy boundary. A schematic of the energy exchange between the very large-scale Reynolds stresses between the mean and wave-induced flows is depicted in Fig. 18.

Interestingly, the mechanism provided here has a potential connection to the studies of Langmuir circulations (LCs) [73] in oceanic turbulence. The sketch of LCs consists of array of elongated vortices parallel to the directions of wind and surface wave propagation, and induces streaks between them [73], similar to the VLSMs over the wavy boundary as shown in Figs. 11 and 12. Teixeira [74] provided a linear model to explain the formation of the LCs based on a rapid-distortion theory. In his work, the turbulent flow is governed by the linearized Craik–Leibovich (C-L) equations [75]. Turbulent structures are streaks of streamwise velocity when the mean flow contains only the shear. While the structures turn to strongly elongated streaks and vortices when a Stokes drift flow is

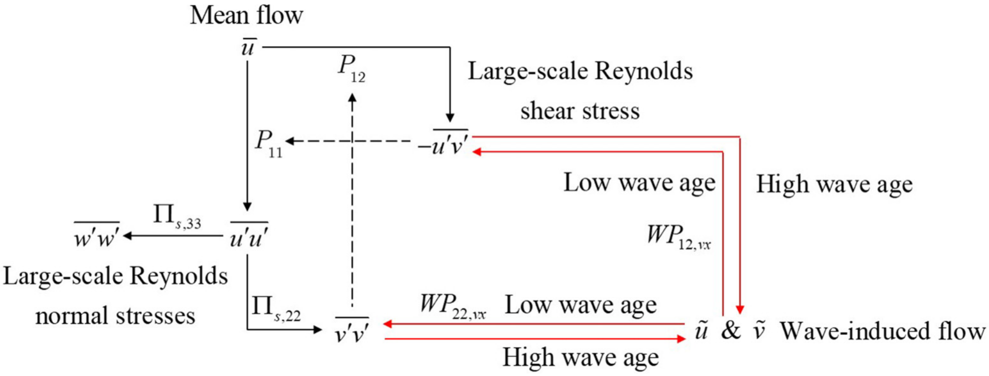

FIG. 18. Sketch of the paths through which the large-scale turbulent fluctuations and momentum flux gain/lose energy.

included in the mean flow. The growth of energy of $\overline{v'v'}$ and $-\overline{u'v'}$ are caused by the so-called "Stokes production." More recently, Deng *et al.* [76] performed LES based on the C-L equations to investigate the Langmuir turbulence. In their work, the Stokes production term induces large magnitude of vertical velocity fluctuation. The Stokes production which represents the nonlinear interaction between the Reynolds stresses and the Stokes drift-induced shear, which are in a similar form with the wave-induced production terms $WP_{22,vx}$ and $WP_{12,vx}$ in the present work.

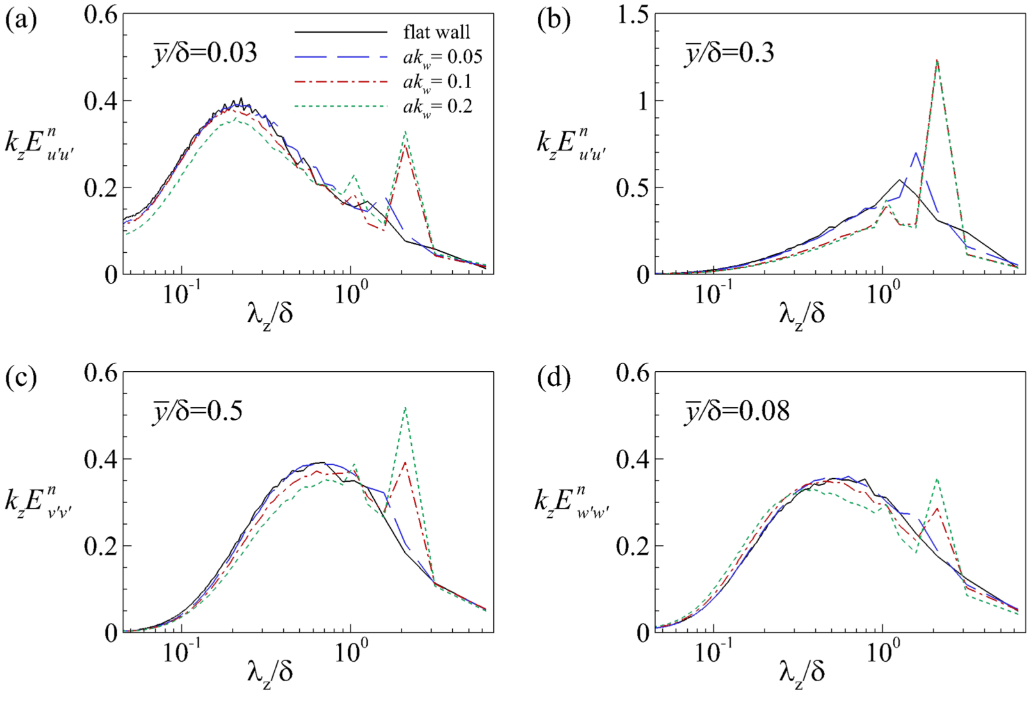

FIG. 19. One-dimensional premultiplied spanwise energy spectra of turbulent velocity fluctuation for different wave steepness: (a) streamwise component u', $\bar{y}/\delta = 0.03$; (b) streamwise component u', $\bar{y}/\delta = 0.3$; (c) vertical component v', $\bar{y}/\delta = 0.5$; (d) spanwise component w', $\bar{y}/\delta = 0.08$.

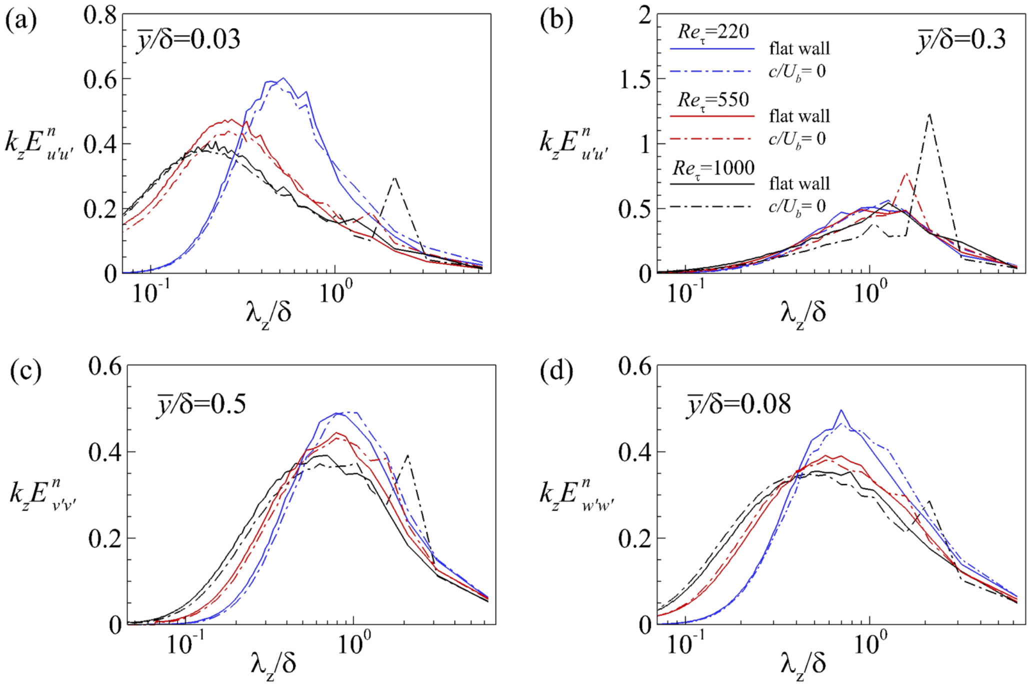

FIG. 20. One-dimensional premultiplied spanwise energy spectra of turbulent velocity fluctuation for different Reynolds numbers: (a) streamwise component u', $\bar{y}/\delta = 0.03$; (b) streamwise component u', $\bar{y}/\delta = 0.3$; (c) vertical component v', $\bar{y}/\delta = 0.5$; (d) spanwise component w', $\bar{y}/\delta = 0.08$.

D. Effects of wave steepness and Reynolds number

In the previous sections, the influence of wavy boundary on the energy distribution among different length scales of turbulent fluctuations was presented, and the attention was mainly paid on the varying wave age. In this section, the effects of the wave steepness and the Reynolds number are further investigated.

According to the previous results, the phenomenon that the enhanced very large-scale turbulent motions and the separation of scales are more significant in the negative wave-age case and the stationary wavy wall case. Here we fix the phase speed $c = 0$ and the wave amplitude $a/\delta = 0.05$, but vary the wavelength k_w to let the wave steepness satisfy $ak_w = 0.05, 0.1,$ and 0.2. For different wave steepnesses, the friction Reynolds number is kept the same, i.e., $\mathrm{Re}_\tau = 1000$. One-dimensional spanwise energy spectra of turbulent velocity fluctuations are shown in Fig. 19 for various wave steepnesses together with the flat-wall case. The vertical locations of the spectra for the streamwise, vertical and spanwise components are same as Fig. 14. As the wave steepness increases, the small-scale energy for the streamwise and vertical velocity components decreases and the very large-scale energy increases. While for the spanwise velocity, both the small-scale and very large-scale energies increase at high wave steepness. The scale of the second peak also increases for the large wave-steepness cases. For the smallest wave-steepness case ($ak_w = 0.05$), the spectra of the streamwise and vertical velocity components are close to the flat-wall case, while the spanwise velocity achieves a second peak at the scale $\lambda_z/\delta = 1.57$. This trend is reasonable because when the wave steepness becomes smaller, the wavy boundary is more similar to the flat wall and the flow is less disturbed by the wave. The small wave steepness also means that the wave-induced fluctuations [Eq. (7)] as well as the wave-induced production terms [Eqs. (18)–(20)] are weak and can hardly alter the energy distribution. It is noted that the variations of intensity and scale with the wave steepness are consistent with Kuhn *et al.* [54]. In addition, their following work indicated that the energy spectra became broader and the spanwise length scale of the flow structures is increased with the blockage ratio [55]. In the present work, we also fix the wavelength $\lambda_w/\delta = \pi$ and change the wave amplitude $a/\delta = 0.025$, 0.05, and 0.1 (or equivalently, $ak_w = 0.05$, 0.1 and 0.2) to estimate the influence of the blockage ratio. It is found that the observed broader spectra and larger turbulent velocity fluctuations (not shown here) agree with those of Zenklusen *et al.* [55].

To investigate the Reynolds number effect, simulations of turbulent flow over the flat and stationary wavy wall at two lower Reynolds numbers, i.e., $\mathrm{Re}_\tau = 220$ and 550 are carried out, as compared with the $\mathrm{Re}_\tau = 1000$ case. All the wave parameters are kept the same for different Reynolds numbers with the wave steepness fixed at $ak_w = 0.1$. The spanwise spectra of turbulent velocity fluctuations are shown in Fig. 20 for different Reynold numbers. For the lowest Reynolds number, i.e., $\mathrm{Re}_\tau = 220$, all the three components of velocity fluctuations in the stationary wavy wall case do not exhibit the scale separation and only a gentle peak exists in the spectra, while the length scale of the only peak for all the three components shifts slightly to the larger scale. Considering the low Reynolds number in this case, the inner- and outer-scales nearly overlap and it is hard to distinguish between them [42]. When the Reynolds number increases to $\mathrm{Re}_\tau = 550$, more distinct differences can be observed in the spectra. The streamwise velocity spectra achieves a second very large-scale peak in both the inner [Fig. 20(a)] and outer [Fig. 20(b)] regions. The shape of the spectra in the very large-scale region ($\lambda_z/\delta > 1$) and outer layer ($\bar{y}/\delta = 0.3$) even coincide with the flat-wall turbulence at a higher Reynolds number $\mathrm{Re}_\tau = 1000$. For the vertical and spanwise components, the spectra also show the scale separation behavior in the stationary wavy wall case. Since the wall turbulence only exhibits a distinct very large-scale peak and scale-separation behavior at high Reynolds numbers, our results indicate that these properties occur at a relatively low Reynolds number and grow with the Reynolds number under the impact of the wavy boundary.

IV. CONCLUSIONS

In the present study, a wall-resolved LES was performed for turbulent flow over the prescribed traveling waves at a friction Reynolds number of $\mathrm{Re}_\tau \approx 1000$. Four different wave ages are considered and compared with the flat-wall turbulence. By applying the triple decomposition [12], the flow fields are decomposed into three components, namely the mean profile, wave-induced fluctuation and turbulent fluctuation. The profiles of mean streamwise velocity for all the wave ages exhibit a logarithmic region along the vertical direction, while both the Karman constant and the intercept of the velocity profile vary with the wave age. The wave-induced stresses are comparable to the Reynolds stresses. Their intensities and spatial distributions are strongly dependent on the wave age. Our results of the wave-induced stresses are consistent with the previous work [27,30]. In contrast, the mean profiles of Reynolds stresses show no significant difference for different wave ages.

The turbulent VLSMs were observed in our simulations. For the flat-wall turbulence, the two peaks in the one-dimensional premultiplied spanwise spectra of the turbulent streamwise velocity correspond to the low-speed streaks in the inner region and the VLSMs in the outer region, respectively. For the negative wave age and the stationary wavy wall cases, the intensity and length scale of the outer peak are increased as compared with the flat-wall case. The spectra of turbulent vertical and spanwise velocities also display additional very large-scale peaks. The enlarged and intensified VLSMs are extracted from the instantaneous and conditionally averaged flow fields. However, the turbulent VLSMs are weakened with the increasing wave age. All the VLSMs extracted by the conditional average involve the elongated low- and high-speed regions in the streamwise direction accompanied by the roll cells, similar with those observed in the flat-wall turbulence at high Reynolds numbers [42]. Effect of the wave steepness was also examined. It was shown that reduction of the small-scale energy and increase of the very large-scale energy in the spectra become more obvious as the wave steepness increases. Moreover, the results at two lower Reynolds numbers indicate that the effect of the wave on the enhancement of the large-scale turbulent motion becomes insignificant as the Reynolds number decreases.

Based on the spectral analysis of the transport equation of two-point velocity correlation, we attempted to explain the wave effect on the VLSMs. It is found that the wave-induced production terms can provide additional energy input to the very large-scale $\overline{v'v'}$ and $\overline{u'v'}$ for the negative wave age and stationary wavy wall cases. Then the very large-scale $\overline{u'u'}$ and $\overline{w'w'}$ are strengthened by the normal production term and pressure-strain term, respectively. The wave-induced production terms reflect the correlation between the wave-induced velocity gradient and the Reynolds stresses. This correlation analysis is similar to Yang and Shen [14], but with an extension to a range of length scales of turbulent fluctuations, which explains the wave effect on enhancement of the VLSMs. As the moving wavy boundary has a wave age of $c/U_b = 0.4$ (or equivalently $c^+ = 7.25$), which lies in the intermediate wave regime [61], the wave-induced flow component is decreased, and thus the related wave-induced production also loses intensity and can hardly alter the energy distribution among different length scales. For the flow over the fast wave, i.e., $c/U_b = 1.2$ ($c^+ = 23.77$), the wave-induced production changes its sign, indicating that the energy begins to transport from the very large-scale motions to the wave-induced flow in this regime.

ACKNOWLEDGMENTS

This work was supported by the National Natural Science Foundation of China under Grants No. 91752205, No. 11772172, and No. 11490551. The authors thank Tsinghua National Laboratory for Information Science and Technology for support in parallel computation. The authors also thank Prof. Lian Shen at the University of Minnesota for instructive discussions.

APPENDIX A: AVERAGE AND DECOMPOSITION OPERATIONS

In the Cartesian coordinate system, the phase average of a physical quantity $f(t, x, y, z)$ can be defined as

$$\langle f\rangle(x, y) \equiv \frac{1}{N_t \times N_w \times L_z} \sum_{n=1}^{N_t} \sum_{m=1}^{N_w} \int_0^{L_z} f(t(n), x + ct(n) + m\lambda_w, y, z)dz, \tag{A1}$$

where L_z is the spanwise width of the computational domain, the indices m, n represent a certain period of the wave at the moment $t(n)$, N_w is the number of the whole wave period contained in the computational domain, and N_t is the number of the instantaneous samples used for average operation. The turbulent component of the quantity's fluctuation is then defined as

$$f'(t, x, y, z) = f(t, x, y, z) - \langle f\rangle(x - ct, y). \tag{A2}$$

Then the time and ξ_2-plane average $\bar{f}$ is obtained by further averaging the phase averaged component along with the curves ξ_1 defined in Eq. (6), i.e.,

$$\bar{f}(\xi_2) = \frac{1}{L_{\xi 1}} \int_0^{L_{\xi 1}} \langle f\rangle d\xi_1 = \frac{1}{L_{\xi 1}} \int_0^{L_{\xi 1}} \langle f\rangle(x(\xi_1), y(\xi_1, \xi_2))d\xi_1. \tag{A3}$$

Here, the axis ξ_2 changes with both x and y, while it can also represent the mean vertical distance from the wave surface $\bar{y}$. Correspondingly, the wave-induced component can be obtained by subtracting the $\bar{f}$ from the phase averaged component, i.e.,

$$\tilde{f}(x, y) = \langle f\rangle(x, y) - \bar{f}(\xi_2(x, y)) = \langle f\rangle(x, y) - \bar{f}(\bar{y}). \tag{A4}$$

APPENDIX B: TRANSPORT EQUATION OF THE TWO-POINT VELOCITY CORRELATION AND ITS SPECTRAL EXPRESSION

The momentum equation of the turbulent velocity fluctuations for the wavy boundary flow can be written as [77]

$$\frac{\partial u_i'}{\partial t} + (\bar{u}_k + \tilde{u}_k)\frac{\partial u_i'}{\partial x_k} = -u_k'\left(\overline{\frac{\partial u_i}{\partial x_k}} + \widetilde{\frac{\partial u_i}{\partial x_k}}\right) - \frac{\partial p'}{\partial x_i} + \frac{1}{\mathrm{Re}}\frac{\partial^2 u_i'}{\partial x_k \partial x_k} - \frac{\partial}{\partial x_k}(u_i'u_k' - \langle u_i'u_k'\rangle) - \frac{\partial \tau_{ik}^{d\,\prime}}{\partial x_k}. \tag{B1}$$

It should be noted that the last term on the right-hand side of Eq. (B1) represents the contribution of the subgrid-scale stress because the data used here is obtained from LES. Then, we define the turbulent fluctuating quantity at the location with a certain distance in the spanwise direction from the reference point, i.e.,

$$f_r' = f'(x, y, z + r_z, t), \tag{B2}$$

where r_z is the separation distance in the spanwise direction. The momentum equation for u_{jr}' can be similarly written as

$$\begin{aligned}\frac{\partial u_{jr}'}{\partial t} + (\bar{u}_k + \tilde{u}_k)\frac{\partial u_{jr}'}{\partial x_k} &= -u_{kr}'\left(\overline{\frac{\partial u_j}{\partial x_k}} + \widetilde{\frac{\partial u_j}{\partial x_k}}\right) - \frac{\partial p_r'}{\partial x_{jr}} + \frac{1}{\mathrm{Re}}\frac{\partial^2 u_{jr}'}{\partial x_{kr}\partial x_{kr}} \\ &\quad - \frac{\partial}{\partial x_{kr}}(u_{jr}'u_{kr}' - \langle u_j'u_k'\rangle) - \frac{\partial \tau_{jk,r}^{d'}}{\partial x_{kr}}.\end{aligned} \tag{B3}$$

By multiplying the u_i' Eq. (B1) by u_{jr}' and the u_{jr}' Eq. (B3) by u_i', and taking the mean after summation, the resulting transport equation of the two-point velocity correlation can be obtained, i.e., Eq. (10).

Furthermore, each term in Eq. (10) can be discretized in the spectral space, i.e.,

$$f(\bar{y}, r_z) = \sum_{k_z} \hat{f}(\bar{y}, k_z)\exp(\mathrm{i}k_z r_z), \tag{B4}$$

where $\hat{f}$ is the spectral coefficient and k_z is the corresponding spanwise wave number. Then, the one-dimensional energy spectra density of f can be defined by the real part of the spectral coefficient, i.e.,

$$E_f(\bar{y}, k_z) = \hat{f}(\bar{y}, k_z) + \hat{f}(\bar{y}, -k_z). \tag{B5}$$

The spectra of the different terms in Eq. (10) depict the energy gain/loss among different length scales and vertical positions.

[1] T. S. Park, H. S. Choi, and K. Suzuki, Nonlinear k–ε–fμ model and its application to the flow and heat transfer in a channel having one undulant wall, Int. J. Heat Mass Transf. **47**, 2403 (2004).

[2] H. S. Choi and K. Suzuki, Large eddy simulation of turbulent flow and heat transfer in a channel with one wavy wall, Int. J. Heat Fluid Flow **26**, 681 (2005).

[3] E. A. Zedler and R. L. Street, Large-eddy simulation of sediment transport: currents over ripples, J. Hydraul. Div. **127**, 444 (2001).

[4] K. Krettenauer and U. Schumann, Numerical simulation of turbulent convection over wavy terrain, J. Fluid Mech. **237**, 261 (1992).

[5] M. S. Triantafyllou, G. S. Triantafyllou, and D. K. P. Yue, Hydrodynamics of fishlike swimming, Annu. Rev. Fluid Mech. **32**, 33 (2000).

[6] L. Shen, X. Zhang, D. K. Yue, and M. S. Triantafyllou, Turbulent flow over a flexible wall undergoing a streamwise traveling wave motion, J. Fluid Mech. **484**, 197 (2003).

[7] R. Nakanishi, H. Mamori, and K. Fukagata, Relaminarization of turbulent channel flow using traveling wave-like wall deformation, Int. J. Heat Fluid Flow **35**, 152 (2012).

[8] J. W. Miles, On the generation of surface waves by shear flows, J. Fluid Mech. **3**, 185 (1957).

[9] O. M. Phillips, On the generation of waves by turbulent wind, J. Fluid Mech. **2**, 417 (1957).

[10] S. E. Belcher and J. C. R. Hunt, Turbulent shear flow over slowly moving waves, J. Fluid Mech. **251**, 109 (1993).

[11] J. E. Cohen and S. E. Belcher, Turbulent shear flow over fast-moving waves, J. Fluid Mech. **386**, 345 (1999).

[12] P. P. Sullivan, J. C. McWilliams, and C. H. Moeng, Simulation of turbulent flow over idealized water waves, J. Fluid Mech. **404**, 47 (2000).

[13] P. P. Sullivan, J. B. Edson, T. Hristov, and J. C. McWilliams, Large-eddy simulations and observations of atmospheric marine boundary layers above nonequilibrium surface waves, J. Atmos. Sci. **65**, 1225 (2008).

[14] D. Yang and L. Shen, Direct-simulation-based study of turbulent flow over various waving boundaries, J. Fluid Mech. **650**, 131 (2010).

[15] T. Hara and P. P. Sullivan, Wave boundary layer turbulence over surface waves in a strongly forced condition, J. Phys. Oceanogr. **45**, 868 (2015).

[16] P. P. Sullivan and J. C. McWilliams, Turbulent flow over water waves in the presence of stratification, Phys. Fluids **14**, 1182 (2002).

[17] Y. I. Troitskaya, E. V. Ezhova, and S. S. Zilitinkevich, Momentum and buoyancy transfer in atmospheric turbulent boundary layer over wavy water surface. Part 1: Harmonic wave, Non. Proc. Geophysics **20**, 825 (2013).

[18] O. A. Druzhinin, Y. I. Troitskaya, and S. S. Zilitinkevich, Stably stratified airflow over a waved water surface. Part 1: Stationary turbulence regime, Q. J. R. Meteorol. Soc. **142**, 759 (2016).

[19] D. Yang and L. Shen, Direct numerical simulation of scalar transport in turbulent flows over progressive surface waves, J. Fluid Mech. **819**, 58 (2017).

[20] Z. Yang, B. Q. Deng, and L. Shen, Direct numerical simulation of wind turbulence over breaking waves, J. Fluid Mech. **850**, 120 (2018).

[21] C. A. Van Duin and P. A. Janssen, An analytic model of the generation of surface gravity waves by turbulent air flow, J. Fluid Mech. **236**, 197 (1992).

[22] C. Mastenbroek, V. K. Makin, M. H. Garat, and J. P. Giovanangeli, Experimental evidence of the rapid distortion of turbulence in the air flow over water waves, J. Fluid Mech. **318**, 273 (1996).

[23] V. K. Makin and V. N. Kudryavtsev, Coupled sea surface-atmosphere model: 1. Wind over waves coupling, J. Geophys. Res.: Oceans **104**, 7613 (1999).

[24] D. Yang, C. Meneveau, and L. Shen, Dynamic modelling of sea-surface roughness for large-eddy simulation of wind over ocean wavefield, J. Fluid Mech. **726**, 62 (2013).

[25] J. B. Edson, V. Jampana, R. A. Weller *et al.*, On the exchange of momentum over the open ocean, J. Phys. Oceanogr. **43**, 1589 (2013).

[26] C. W. Fairall, E. F. Bradley, J. E. Hare, A. A. Grachev, and J. B. Edson, Bulk parameterization of air–sea fluxes: Updates and verification for the COARE algorithm, J. Clim. **16**, 571 (2003).

[27] P. P. Sullivan and J. C. McWilliams, Dynamics of winds and currents coupled to surface waves, Annu. Rev. Fluid Mech. **42**, 19 (2010).

[28] N. Kihara, H. Hanazaki, T. Mizuya, and H. Ueda, Relationship between airflow at the critical height and momentum transfer to the traveling waves, Phys. Fluids **19**, 015102 (2007).

[29] Q. Jiang, P. Sullivan, S. Wang, J. Doyle, and L. Vincent, Impact of swell on air–sea momentum flux and marine boundary layer under low-wind conditions, J. Atmos. Sci. **73**, 2683 (2016).

[30] M. P. Buckley and F. Veron, Structure of the airflow above surface waves, J. Phys. Oceanogr. **46**, 1377 (2016).

[31] D. Yang and L. Shen, Characteristics of coherent vortical structures in turbulent flows over progressive surface waves, Phys. Fluids **21**, 125106 (2009).

[32] H. S. Choi, T. S. Park, and K. Suzuki, Turbulence characteristics of the flows in a wavy channel, Int. J. Transp. Phenom. **6**, 197 (2004).

[33] Y. H. Tseng and J. H. Ferziger, Large-eddy simulation of turbulent wavy boundary flow-illustration of vortex dynamics, J. Turbul. **5**, 1 (2004).

[34] C. Wagner, S. Kenjereš, and P. R. von Rohr, Dynamic large eddy simulations of momentum and wall heat transfer in forced convection over wavy surfaces, J. Turbul. **12**, N7 (2011).

[35] S. K. Robinson, Coherent motions in the turbulent boundary layer, Annu. Rev. Fluid Mech. **23**, 601 (1991).

[36] J. Kim, P. Moin, and R. Moser, Turbulence statistics in fully developed channel flow at low Reynolds number, J. Fluid Mech. **177**, 133 (1987).

[37] J. Jeong, F. Hussain, W. Schoppa, and J. Kim, Coherent structures near the wall in a turbulent channel flow, J. Fluid Mech. **332**, 185 (1997).

[38] K. C. Kim and R. J. Adrian, Very large-scale motion in the outer layer, Phys. Fluids **11**, 417 (1999).

[39] N. Hutchins, and I. Marusic, Evidence of very long meandering features in the logarithmic region of turbulent boundary layers, J. Fluid Mech. **579**, 1 (2007a).

[40] J. H. Lee and H. J. Sung, Very-large-scale motions in a turbulent boundary layer, J. Fluid Mech. **673**, 80 (2011).

[41] B. J. Balakumar and R. J. Adrian, Large-and very-large-scale motions in channel and boundary-layer flows, Philos. Trans. R. Soc., A **365**, 665 (2007).

[42] N. Hutchins and I. Marusic, Large-scale influences in near-wall turbulence, Philos. Trans. R. Soc., A **365**, 647 (2007b).

[43] R. Mathis, N. Hutchins, and I. Marusic, Large-scale amplitude modulation of the small-scale structures in turbulent boundary layers, J. Fluid Mech. **628**, 311 (2009).

[44] D. Chung and B. J. McKeon, Large-eddy simulation of large-scale structures in long channel flow, J. Fluid Mech. **661**, 341 (2010).

[45] J. Komminaho, A. Lundbladh, and A. V. Johansson, Very large structures in plane turbulent Couette flow, J. Fluid Mech. **320**, 259 (1996).

[46] V. Avsarkisov, S. Hoyas, M. Oberlack, and J. P. García-Galache, Turbulent plane Couette flow at moderately high Reynolds number, J. Fluid Mech. **751**, R1 (2014).

[47] M. Lee and R. D. Moser, Extreme-scale motions in turbulent plane Couette flows, J. Fluid Mech. **842**, 128 (2018).

[48] V. De Angelis, P. Lombardi, and S. Banerjee, Direct numerical simulation of turbulent flow over a wavy wall, Phys. Fluids **9**, 2429 (1997).

[49] D. S. Henn and R. I. Sykes, Large-eddy simulation of flow over wavy surfaces, J. Fluid Mech. **383**, 75 (1999).

[50] W. Gong, P. A. Taylor, and A. Dörnbrack, Turbulent boundary-layer flow over fixed aerodynamically rough two-dimensional sinusoidal waves, J. Fluid Mech. **312**, 1 (1996).

[51] A. Günther and P. R. Von Rohr, Large-scale structures in a developed flow over a wavy wall, J. Fluid Mech. **478**, 257 (2003).

[52] N. Kruse, A. Günther, and P. R. Von Rohr, Dynamics of large-scale structures in turbulent flow over a wavy wall, J. Fluid Mech. **485**, 87 (2003).

[53] N. Kruse, S. Kuhn, and P. R. von Rohr, Wavy wall effects on turbulence production and large-scale modes, J. Turbul. **7**, N31 (2006).

[54] S. Kuhn, C. Wagner, and P. R. von Rohr, Influence of wavy surfaces on coherent structures in a turbulent flow, Exp. Fluids **43**, 251 (2007).

[55] A. Zenklusen, S. Kuhn, and P. R. von Rohr, Structural dissimilarity of large-scale structures in turbulent flows over wavy walls, Phys. Fluids **24**, 055112 (2012).

[56] E. O. Nilsson, A. Rutgersson, A. S. Smedman, and P. P. Sullivan, Convective boundary-layer structure in the presence of wind-following swell, Q. J. R. Meteorol. Soc. **138**, 1476 (2012).

[57] P. P. Sullivan, J. C. McWilliams, and E. G. Patton, Large-eddy simulation of marine atmospheric boundary layers above a spectrum of moving waves, J. Atmos. Sci. **71**, 4001 (2014).

[58] M. Lee, Direct numerical simulation (DNS) for incompressible turbulent channel flow at $\mathrm{Re}_\tau = 5200$ Ph.D. dissertation, The University of Texas at Austin, Austin, Texas, 2015.

[59] M. Germano, U. Piomelli, P. Moin, and W. H. Cabot, A dynamic subgrid-scale eddy viscosity model, Phys. Fluids A **3**, 1760 (1991).

[60] D. K. Lilly, A proposed modification of the Germano subgrid-scale closure method, Phys. Fluids A **4**, 633 (1992).

[61] S. E. Belcher and J. C. R. Hunt, Turbulent flow over hills and waves, Annu. Rev. Fluid Mech. **30**, 507 (1998).

[62] S. Kang and H. Choi, Active wall motions for skin-friction drag reduction, Phys. Fluids **12**, 3301 (2000).

[63] M. W. Ge, C. X. Xu, and G. X. Cui, Direct numerical simulation of flow in channel with time-dependent wall geometry, Appl. Math. Mech. **31**, 97 (2010).

[64] G. E. Karniadakis, M. Israeli, and S. A. Orszag, High-order splitting methods for the incompressible Navier-Stokes equations, J. Comput. Phys. **97**, 414 (1991).

[65] J. C. del Álamo and J. Jiménez, Spectra of the very large anisotropic scales in turbulent channels, Phys. Fluids **15**, L41 (2003).

[66] C. D. Tomkins and R. J. Adrian, Energetic spanwise modes in the logarithmic layer of a turbulent boundary layer, J. Fluid Mech. **545**, 141 (2005).

[67] M. Bernardini and S. Pirozzoli, Inner/outer layer interactions in turbulent boundary layers: a refined measure for the large-scale amplitude modulation mechanism, Phys. Fluids **23**, 061701 (2011).

[68] H. Abe, H. Kawamura, and H. Choi, Very large-scale structures and their effects on the wall shear-stress fluctuations in a turbulent channel flow up to $\mathrm{Re}\tau = 640$, J. Fluids Eng. **126**, 835 (2004).

[69] K. Iwamoto, N. Kasagi, and Y. Suzuki, Dynamical roles of large-scale structures in turbulent channel flow, Comput. Mech. **4**, 5 (2004).

[70] K. Fukagata, M. Kobayashi, and N. Kasagi, On the friction drag reduction effect by a control of large-scale turbulent structures, J. Fluid Sci. Tech. **5**, 574 (2010).

[71] M. Lee and R. D. Moser, Spectral analysis on Reynolds stress transport equation in high Firewall-bounded turbulence, in *International Symposium on Turbulence and Shear Flow Phenomena (TSFP-9), Melbourne* (Begell House, 2015), p. 4A–3.

[72] M. Lee and R. D. Moser, Role of large scale motions in turbulent Poiseuille and Couette flows, in *International Symposium on Turbulence and Shear Flow Phenomena (TSFP-10), Chicago* (http://tsfp10.org/TSFP10_program/_program.html, 2017), pp. 9B–3.

[73] S. A. Thorpe, Langmuir circulation, Annu. Rev. Fluid Mech. **36**, 55 (2004).

[74] M. A. Teixeira, A linear model for the structure of turbulence beneath surface water waves, Ocean Modelling **36**, 149 (2011).

[75] S. Leibovich, On the evolution of the system of wind drift currents and Langmuir circulations in the ocean. Part 1. Theory and averaged current, J. Fluid Mech. **79**, 715 (1977).

[76] B. Q. Deng, Z. Yang, A. Xuan, and L. Shen, Influence of Langmuir circulations on turbulence in the bottom boundary layer of shallow water, J. Fluid Mech. **861**, 275 (2019).

[77] W. C. Reynolds and A. K. M. F. Hussain, The mechanics of an organized wave in turbulent shear flow. Part 3. Theoretical models and comparisons with experiments, J. Fluid Mech. **54**, 263 (1972).